# NAC guides a ribosomal multienzyme complex for nascent protein processing

https://doi.org/10.1038/s41586-024-07846-7

Received: 18 November 2023

Accepted: 18 July 2024

Published online: 21 August 2024



Check for updates

Alfred M. Lentzsch<sup>1,4</sup>, Denis Yudin<sup>2,4</sup>, Martin Gamerdinger<sup>3</sup>, Sowmya Chandrasekar<sup>1</sup>, Laurenz Rabl<sup>3</sup>. Alain Scaiola<sup>2</sup>. Elke Deuerling<sup>3</sup>. Nenad Ban<sup>2™</sup> & Shu-ou Shan<sup>1™</sup>

Approximately 40% of the mammalian proteome undergoes N-terminal methionine excision and acetylation, mediated sequentially by methionine aminopeptidase (MetAP) and N-acetyltransferase A (NatA), respectively<sup>1</sup>. Both modifications are strictly cotranslational and essential in higher eukaryotic organisms<sup>1</sup>. The interaction, activity and regulation of these enzymes on translating ribosomes are poorly understood. Here we perform biochemical, structural and in vivo studies to demonstrate that the nascent polypeptide-associated complex<sup>2,3</sup> (NAC) orchestrates the action of these enzymes. NAC assembles a multienzyme complex with MetAP1 and NatA early during translation and pre-positions the active sites of both enzymes for timely sequential processing of the nascent protein. NAC further releases the inhibitory interactions from the NatA regulatory protein huntingtin yeast two-hybrid protein K<sup>4,5</sup> (HYPK) to activate NatA on the ribosome, enforcing cotranslational N-terminal acetylation. Our results provide a mechanistic model for the cotranslational processing of proteins in eukaryotic cells.

N-terminal acetylation is a ubiquitous modification that occurs on 80% of the human proteome<sup>1,6</sup> and affects protein folding<sup>7</sup>, interaction<sup>8,9</sup>, localization<sup>10</sup>, half-life<sup>11,12</sup> and aggregation propensity<sup>13-15</sup>. Dysregulation of N-terminal acetylation has been linked to severe developmental syndromes<sup>16,17</sup>, cancer<sup>18,19</sup> and Parkinson's disease<sup>20,21</sup>. N-terminal acetylation is carried out by eight classes of N-terminal acetyltransferases<sup>1,22</sup>, most of which act cotranslationally on nascent proteins as they emerge from the polypeptide exit tunnel of the ribosome<sup>23-26</sup>. Among them, NatA mediates 50% of N-terminal acetylation<sup>1</sup>, with a specificity for N termini containing a small amino acid (A, S, T, V, C or G) after the initiator methionine (iMet) is excised by MetAPs<sup>1,6,27</sup>. NatA is a protein complex comprising the catalytic subunit Naa10 and the auxiliary subunit Naa15<sup>22,28</sup>. An additional catalytic subunit Naa50, which contains an active site for acetylation of iMet-containing nascent chains (NatE activity), can further bind Naa15 to form a multienzyme complex referred to as NatA/E<sup>22</sup>. Despite the cotranslational nature of N-terminal acetylation, how mammalian NatA/E complexes are recruited to and act on nascent proteins on the ribosome is poorly understood. MetAP1 and NatA must sequentially process the nascent chain within a limited time window during translation, but the timing of their actions is unknown. Finally, the catalytic activity of NatA is controlled by HYPK, which inhibits NatA in vitro<sup>5,29,30</sup> but paradoxically enhances NatA activity in vivo<sup>4,31,32</sup>, suggesting that an unknown mechanism regulates NatA interaction and activity in the context of its in vivo binding partners. Here we resolve these questions and explain how cotranslational protein acetylation by NatA is coordinated with MetAP1 and spatiotemporally controlled by NAC, a ubiquitous ribosome-associated complex that is essential for protein biogenesis.

#### NAC recruits NatA/E to the ribosome

To understand how mammalian NatA is recruited to translating ribosomes, we developed an assay based on Förster resonance energy transfer (FRET). We generated ribosome-nascent chain complexes by in vitro translation of mRNAs lacking a stop codon in rabbit reticulocyte lysate (RRL). The stalled ribosome-nascent chain complex (RNC) bearing the N-terminal 53 amino acids of RPL4 (also known as uL4) (RNC<sub>RPL4</sub>), a NatA substrate, was labelled with BODIPY-FL (Extended Data Fig. 1a). To capture the pre-chemistry steps in the enzymatic reaction cycle, recombinant human NatA bearing catalytically inactivating mutations at the Naa10 active site was labelled near the N terminus with a FRET acceptor (Extended Data Fig. 1d-g). Initial experiments with purified RNC<sub>RPI 4</sub> and NatA detected only weak binding (Fig. 1a,b, blue), consistent with previous ribosome co-sedimentation studies<sup>24</sup>.

We therefore considered other factors that could modulate binding. A candidate for this role is NAC, a conserved protein complex that is bound at the ribosome exit site during early stages of translation<sup>2,3</sup>. NAC comprises a central globular domain formed by dimerization of  $NAC\alpha$  and  $NAC\beta$  subunits, and flexible N- and C-terminal tails that are used for a range of interactions with protein biogenesis factors<sup>33–35</sup>. For example, the flexibly tethered C-terminal ubiquitin-associated domain (UBA) in NACa recruits signal recognition particle (SRP) for cotranslational protein targeting<sup>33,36</sup>.

In support of this hypothesis, efficient FRET (30-50%) was observed between NAC-bound RNC<sub>RPL4</sub> and NatA (Fig. 1a, red). Equilibrium titrations showed high-affinity binding of NatA to RNC<sub>RPL4</sub> only in the presence of NAC, with an equilibrium dissociation constant  $(K_d)$  of less than 1 nM (Fig. 1a,b, red). The same affinity was measured for the human

Division of Chemistry and Chemical Engineering, California Institute of Technology, Pasadena, CA, USA. 2Department of Biology, Institute of Molecular Biology and Biophysics, ETH Zurich, Zurich, Switzerland. 3Department of Biology, Molecular Microbiology, University of Konstanz, Konstanz, Germany. 4These authors contributed equally: Alfred M. Lentzsch, Denis Yudin. <sup>™</sup>e-mail: ban@mol.biol.ethz.ch: sshan@caltech.edu

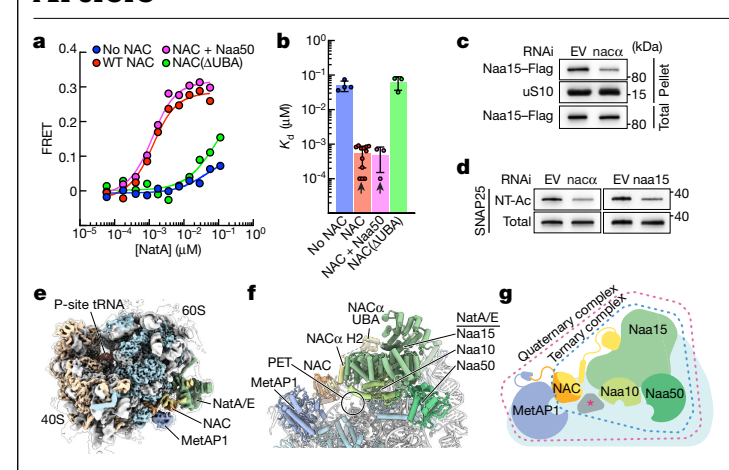


Fig. 1| The NACα UBA domain recruits NatA/E to the ribosome. a, Equilibrium titrations to measure RNC-NatA binding affinity. Titrations contained 1 nM  $BODIPY-FL-labelled\,RNC_{RPL4}, indicated\,concentrations\,of\,tetramthylrhodamine$ labelled Naa15/Naa10(E24Q/Y26F) (NatA) and 50 nM wild-type (WT) NAC or NAC( $\Delta$ UBA) and 500 nM Naa50 as indicated. **b**, Summary of the  $K_d$  values of the RNC-NatA complex. Data are mean  $\pm$  s.d., with n = 4 (no NAC), 12 (wild-type NAC), 3 (+Naa50) and 3 (NAC(ΔUBA)) independent measurements. Black arrows indicate that the  $K_d$  value reached fitting limit.  $\mathbf{c}$ , Ribosome association of NatA after knockdown of NAC $\alpha$  (encoded by icd-2, knockdown indicated as nac $\alpha$ ) in C. elegans. The Flag-tagged NatA subunit Naa15 was detected by immunoblotting in the total and ribosomal pellet fractions. Empty vector (EV) served as a control. RNAi, RNA-mediated interference. d, N-terminal acetylation of a NatA model substrate (SNAP25) after knockdown of NAC $\alpha$  (nac $\alpha$ ) or Naa15 (naa15) in C. elegans. The N-terminally acetylated (NT-Ac) substrate was detected with an epitope-specific antibody. Representative immunoblots in c,d. Experiments were repeated three times. **e**, Overview of the cryo-EM map of RNC<sub>RPI 4</sub> in the quaternary complex with NAC, MetAP1 and NatA/E. The map was lowpassfiltered to estimated local resolution; the black outline shows the same map lowpass-filtered to 8 Å resolution. f, Top view of the quaternary complex model showing how NAC positions nascent chain-processing enzymes around the opening of the ribosomal polypeptide exit tunnel (PET). g, Schematic representation of ternary and quaternary complexes on the 60S subunit (light blue) and the position of the nascent chain in the polypeptide exit tunnel (dark grey) indicated as an asterisk. The following colours are used throughout: rRNA, light grey; 40S ribosomal proteins, beige; 60S ribosome proteins, light blue; P-site tRNA, red; NACα, yellow; NACβ, orange; MetAP1, slate blue; NatA/E, green shades.

NatA/E complex that additionally includes the Naa50 subunit (Fig. 1a,b, purple), suggesting that human Naa50 does not make additional stabilizing interactions with the ribosome  $^{26}$ . NatA–RNC  $_{\text{RPL4}}$  binding was around 100-fold weaker upon deletion of the UBA domain in NAC  $\alpha$  (NAC( $\Delta$ UBA); Fig. 1a,b, green), indicating an essential role of the UBA domain in recruiting NatA to ribosomes. These findings also indicate the formation of a high-affinity ternary complex between RNC, NAC and NatA/E, which is corroborated by the observation of RNC-induced FRET between the NAC  $\alpha$  UBA domain and NatA (Extended Data Fig. 1h,i).

Consistent with the biochemical measurements, the ribosome association of NatA was strongly decreased in *Caenorhabditis elegans* and human cells after knockdown of NAC (Fig. 1c and Extended Data Fig. 2a). Moreover, N-terminal acetylation of the NatA model substrate SNAP25 $^{\rm 37}$  was severely impaired in vivo upon knockdown of NAC, similar to knockdown of the NatA subunit Naa15 (Fig. 1d). These data suggest that the ribosome interaction and function of NatA depends on NAC in vivo.

#### A cotranslational multienzyme complex

To understand how NAC promotes NatA/E-ribosome binding, we used single-particle cryo-electron microscopy (cryo-EM) to solve the structure of the ternary complex comprising RNC  $_{\rm RPL4}$  bearing a 53-amino-acid

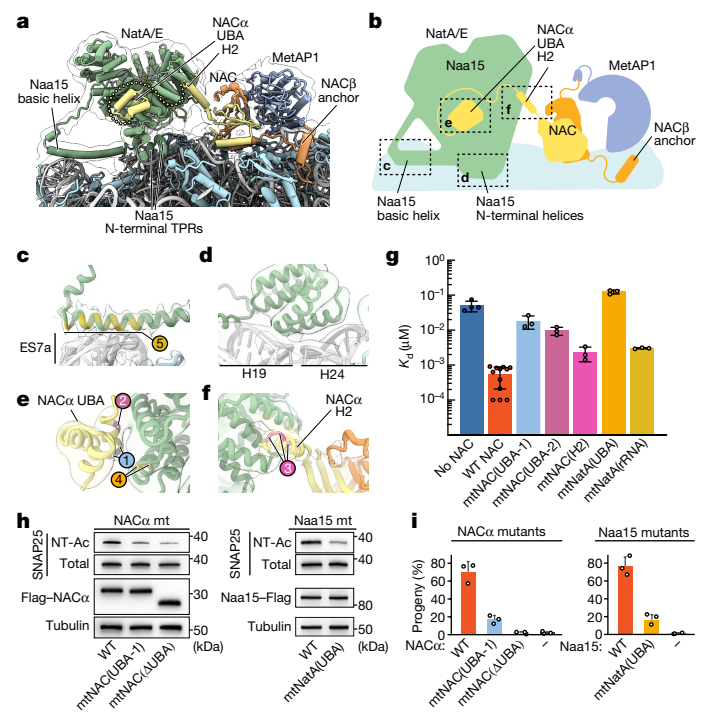


Fig. 2 | NatA interacts with RNC via a combination of ribosome and NAC contacts. a, Overview of the quaternary complex, highlighting key interactions between NatA/E, the ribosome and NAC. The yellow dotted line depicts the flexible linker between NAC $\alpha$  H2 and UBA. The outline shows the homogeneously refined cryo-EM map lowpass-filtered to 8 Å resolution. b, Schematic of the quaternary complex. Rectangles highlight key contacts shown in c-f. c-f, Magnified views of key contacts in the ternary complex structure: the Naa15 basic helix docks onto ES7a of the 28S rRNA (c): the Naa15 N-terminal helical bundle contacts H19 and H24 of the 28S rRNA (d); the UBA (e) and H2 ( $\mathbf{f}$ ) of NAC $\alpha$  contact N-terminal TPRs of Naa15. The outline shows the homogeneously (c,f; lowpass-filtered to 5 Å resolution) or locally (d,e) refined cryo-EM maps. The residues that were biochemically tested are coloured and numbered as in  $\mathbf{g}$ ,  $\mathbf{g}$ , Summary of the  $K_d$  values for RNC-NatA binding with the indicated mutations in NAC $\alpha$  or NatA. Details of the mutations are listed in Extended Data Table 2. Values are obtained from titrations in Extended Data Fig. 6. Individual data points are shown, and values represent mean  $\pm$  s.d.; n = 3independent measurements. The data without NAC and with wild-type NAC are from Fig. 1 and shown for comparison, h. N-terminal acetylation of a NatA model substrate (SNAP25) in C. elegans expressing the indicated Flag-tagged  $NAC\alpha$  (left) or Naa15 (right) variants in the endogenous  $NAC\alpha$  or Naa15 RNAi background. N-terminally acetylated substrate was detected by an epitopespecific antibody. i, Viability of the same worms used in h. Graph shows the number of progeny in each mutant strain relative to wild-type worms (set to 100%). Data are mean  $\pm$  s.d.; n = 3 biological replicates.

nascent chain, NAC and catalytically inactive NatA/E (Extended Data Fig. 4). In addition, we further structurally investigated whether the upstream enzyme MetAP1 co-binds with NatA/E and NAC on the RNC. Co-binding may be possible, since MetAP1 was recently found to be recruited to the ribosome by the C-terminal tail of NAC $\beta^{34}$ , whereas NatA/E is recruited by the UBA domain of NAC $\alpha$  as shown above. We used catalytically impaired variants of MetAP1 and NatA/E to capture the enzyme complex prior to chemistry. Both structures were solved to overall resolutions of 3–4 Å (Extended Data Table 1 and Extended Data Fig. 3). The cryo-EM maps show stalled translating ribosomes with NAC, NatA/E and MetAP1 bound at the polypeptide tunnel exit on the large ribosomal subunit. In both cases, the nascent polypeptide chain could be traced throughout the exit tunnel of the ribosome but not outside it. NatA/E, MetAP1 and NAC had local resolutions of 6–10 Å (Extended Data Fig. 3), enabling us to confidently dock known

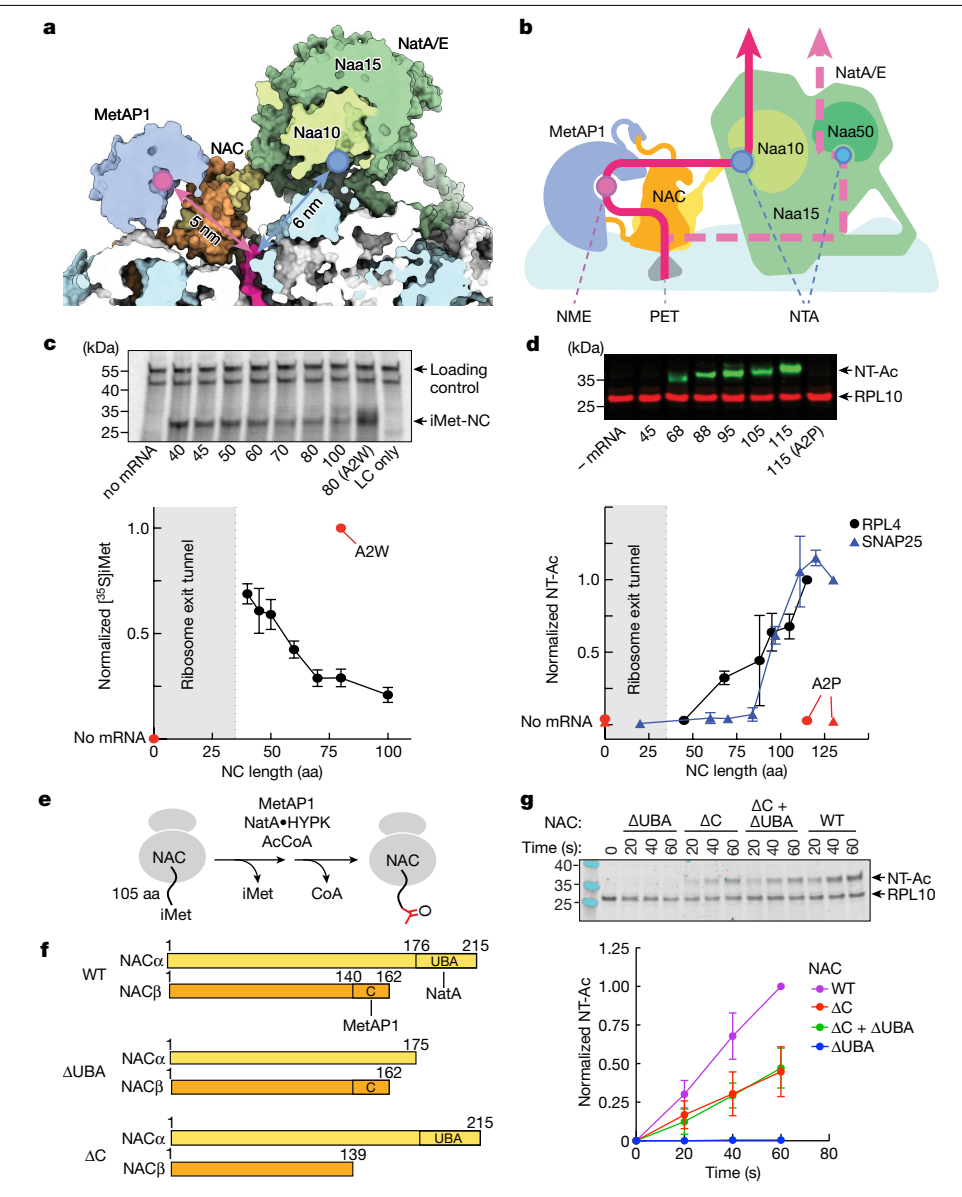


Fig. 3 | MetAP1 and NatA co-bind on the RNC and sequentially modify the nascent chain. a, Back view of the quaternary complex model in surface representation. The clipping plane goes through the polypeptide exit tunnel and the active sites of MetAP1 and Naa10, the catalytic subunits of NatA. Pink and blue circles mark the positions of MetAP1 and NatA active sites, respectively, arrows indicate the distance between these active sites and the opening of the polypeptide exit tunnel. b, In the corresponding cartoon representation of the quaternary complex, the solid pink arrow indicates the path of the nascent chain N termini that first has its iMet excised by MetAP1 and then is acetylated by NatA. The dashed pink arrow shows the hypothetical path of nascent chain N termini that are not cleaved by MetAP1 and have their iMet acetylated by Naa50 (NatE) instead. NME, N-terminal methionine excision; NTA, N-terminal acetylation. c,d, Measurements of the timing of iMet excision (c) and

N-terminal acetylation (d) in RRL using stalled RNCs with the indicated  $nascent\, chain\, (NC)\, lengths.\, iMet\, cleavage\, was\, visualized\, by\, SDS-PAGE\, and\, lengths.\, iMet\, cleavage\, was\, visualized\, by\, SDS-PAGE\, and\, lengths.\, lengths\, lengths$ autoradiography. N-terminal acetylation was detected by western blot using the SMI81 antibody. Skd3-eGFP and RPL10 (also known as uL16) served as the loading control (LC) in c and d, respectively. RNCs with Trp or Pro as the second residue (A2W or A2P), which are not processed by either enzyme, served as negative controls, e. Scheme of the coupled iMet excision and N-terminal acetylation reaction shown in g. Details of reaction conditions are in Methods. f, Domain diagrams of the NAC variants used in g. Arrows denote motifs involved in enzyme recruitment. g, Representative western blot (top) and time courses (bottom) of the coupled iMet excision and N-terminal acetylation reactions mediated by MetAP1, NatA and the indicated NAC variants. Data in  $\mathbf{c}$ ,  $\mathbf{d}$ ,  $\mathbf{g}$  are mean  $\pm$  s.d. from four independent measurements.

structures of NAC, NatA/E and MetAP1. Contact points of NatA/E with the ribosome and with NAC were resolved sufficiently well in some regions to enable molecular modelling of secondary structure. The conformation of NatA/E and its interactions with the ribosome are the same in the ternary and the MetAP1-containing quaternary complexes (Figs. 1f and 2a and Extended Data Fig. 4). While processing the cryo-EM data collected on the ternary complex sample, we also identified a set of non-translating ribosomes with NAC-NatA/E bound (Supplementary Fig. 2). By performing a NatA/E-focused 3D classification on this broader set of data (Supplementary Fig. 3), we could select a stack of conformationally homogeneous particles to reconstruct a map of the ternary 80S-NAC-NatA/E complex with better-resolved NatA/E (Supplementary Fig. 3b-e). The structure and interactions of NatA/E in the 80S-NAC-NatA/E complex are the same as for the RNC  $_{\rm RPL4}$ -NAC-NatA/E ternary complex, which we focus on below.

NAC binds the ribosome in the same configuration as previously observed<sup>33,34</sup>, with the N-terminal basic motif of NACβ anchored at eL19 and eL22 and the NAC globular domain at the tunnel exit (Fig. 2a). NatA/E binds next to the NAC globular domain via specific contacts with NAC and with the surface of the large ribosomal subunit (Fig. 2a,b).

Specifically, the internal basic helix of Naa15, previously observed to be flexibly disposed 5.26.29, becomes ordered upon binding the ribosomal RNA (rRNA) expansion segment 7a (ES7a) via multiple basic residues (Fig. 2c). In addition, two N-terminal helices of Naa15 contact 28S rRNA helices H19 and H24 (Fig. 2d), as previously suggested in biochemical studies 24.25.

We observed two additional regions of density around the N-terminal tetratricopeptide repeats (TPRs) of Naa15: a density resembling a three-helix bundle and a tubular density connecting to the globular domain of NAC, suggesting the bound segments of NACα (Fig. 2a,e,f and Extended Data Fig. 4). Aided by the AlphaFold2-multimer prediction<sup>38,39</sup> of the Naa15-NACα complex (Extended Data Fig. 4f-h), we modelled these densities as the NACα C-terminal UBA domain and a helix in NACα that follows the NAC globular domain (termed H2). The bipartite interactions suggest distinct roles of these NACα regions in recruitment of NatA/E: the UBA domain captures the enzyme complex, whereas H2 helps position it near the polypeptide exit tunnel of the ribosome. Of note, these structures reveal a different mode of ribosome binding for the mammalian NatA/E determined here compared with that of yeast NatA/E<sup>26</sup>, suggesting an evolutionary divergence of the ribosome recruitment mechanisms for protein biogenesis factors (Extended Data Fig. 5).

We carried out structure-guided mutagenesis to test the functional relevance of the observed contacts of NatA with NAC and with the ribosome in vitro and in vivo. To analyse the role of the NAC UBA domain interaction in NatA-ribosome binding, two NAC variants carrying mutations in a hydrophobic patch in the C-terminal  $\alpha$ -helix of NAC $\alpha$  UBA domain (mtNAC(UBA-1) and mtNAC(UBA-2); Extended Data Table 2) were investigated in vitro (Fig. 2e). Both mutations weakened NatA binding to RNC  $_{\rm RPL4}$  by 10- to 20-fold (Fig. 2g and Extended Data Fig. 6). Reciprocally, mutation of residues L73A/L77A of Naa15, which contact the NAC $\alpha$  UBA domain (mtNatA(UBA)), weakened RNC binding affinity by around 100-fold (Fig. 2g and Extended Data Fig. 6b).

Mutations at other surfaces of the UBA domain of NAC $\alpha$  had modest or no effects (Extended Data Fig. 6), attesting to the specificity of the interaction interface. Thus, the hydrophobic interaction of the NAC $\alpha$  UBA domain with Naa15 drives high affinity NatA binding to ribosomes. In contrast to this high affinity binding site, more modest (3- to 4-fold) binding defects were observed with mutations designed to disrupt the Naa15–NAC $\alpha$  H2 contact (mtNAC(H2); Fig. 2g, Extended Data Fig. 6 and Extended Data Table 2). Mutation of NatA contacts with the ribosome via the long positively charged helix of Naa15 (mtNatA(rRNA); Fig. 2g and Extended Data Fig. 6) also had a modest effect (3- to 4-fold). These results indicate that high-affinity NatA interaction with the ribosome is mediated predominantly through the flexibly disposed UBA domain of NAC, and that the electrostatic contacts of the positively charged helix in NatA with rRNA near the polypeptide tunnel exit optimally position the enzyme for nascent chain interactions.

Consistent with the biochemical data, the ribosome association of NatA was strongly decreased in human cells upon mutation of the Naa15–NAC $\alpha$  UBA binding interface (Extended Data Fig. 2). Moreover, N-terminal acetylation of a model NatA substrate was strongly reduced in *C. elegans* upon disruption of the Naa15–NAC $\alpha$  UBA interaction (Fig. 2h). Finally, the viability of the worms was also severely impaired (Fig. 2i). Therefore, the hydrophobic interaction of the UBA domain of NAC $\alpha$  with Naa15 is essential for NatA–ribosome binding and function in vivo.

#### Coordinated MetAP1 and NatA reactions

The structure of the quaternary complex reveals that NatA/E is positioned next to the NAC globular domain, with the active sites of both catalytic subunits (Naa10 and Naa50) pointing towards the polypeptide tunnel (Figs. 1f and 3a). MetAP1 is positioned across the NAC globular domain from NatA/E (Figs. 1f, 2a and 3a) and is

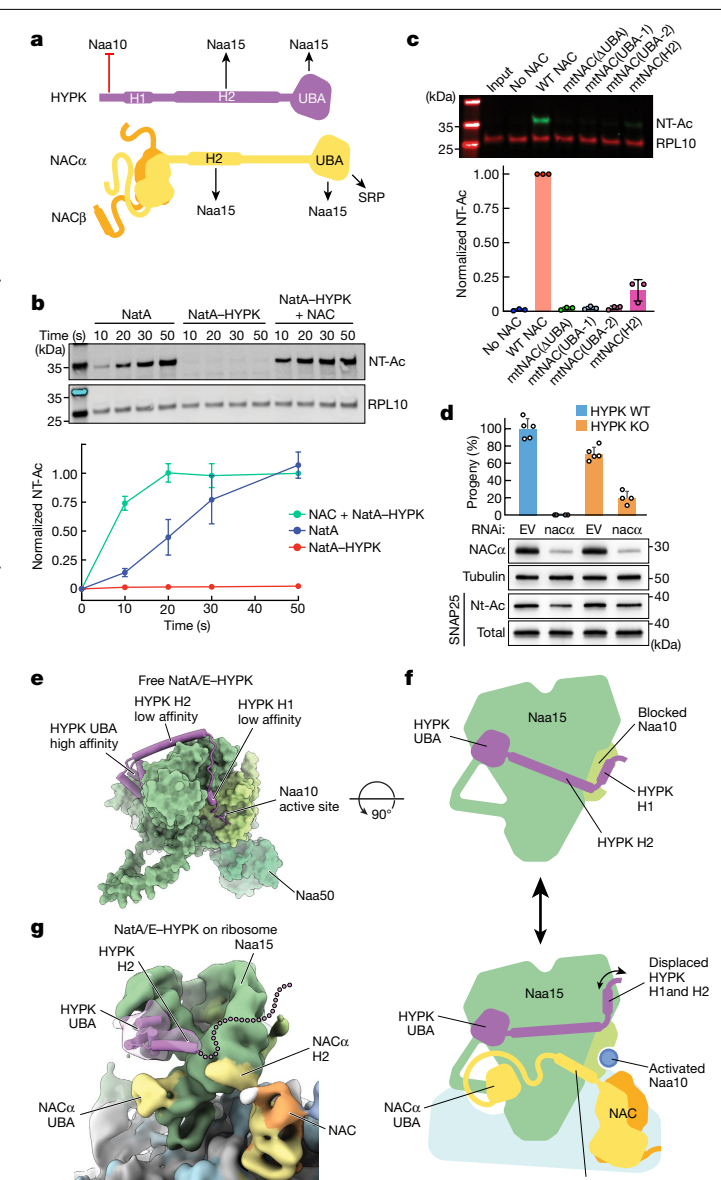


Fig. 4 | NAC activates NatA-HYPK on the ribosome. a, Scheme depicting the domain organization of HYPK and NAC, with arrows depicting the interaction partners for individual domains. b, Reconstituted N-terminal acetylation reactions on RNC. Top, representative western blot of reaction time courses. Bottom, quantification of the data from three independent measurements, shown as mean  $\pm$  s.d.  $\mathbf{c}$ , Reconstituted N-terminal acetylation reactions on RNC with NatA-HYPK and the indicated NAC variants. Reactions were quenched at 60 s. Top, representative western blot. Bottom, quantification of data from three independent measurements. Individual data points are shown, and values represent mean  $\pm$  s.d. **d**, Top, viability of NAC $\alpha$  RNAi worms in wild-type  $HYPK and \, HYPK\text{-}knockout \, (KO) \, background. \, The \, graph \, shows \, the \, number \, of \, and \, background \, decreases \, and \, background \, decreases \, decre$ progeny relative to empty vector RNAi wild-type worms (set to 100%). Data are mean  $\pm$  s.d.; n = 3 biological replicates. Bottom, immunoblots showing NAC $\alpha$ knockdown efficiency in each strain and N-terminal acetylation of the NatA model substrate SNAP25. The N-acetylated substrate was detected by an epitope-specific antibody. e, Model of HYPK (purple) bound to free NatA/E (green). HYPK was modelled onto the quaternary complex by superposition of free NatA-HYPK (Protein Data Bank (PDB) 6C95). f, Cartoon of free NatA-HYPK (top) and NatA-HYPK recruited by NAC at the ribosome (bottom), summarizing the mechanism of HYPK derepression by NAC, as described in the text. The blue circle indicates the unblocked active site of Naa10. g, Cryo-EM structure of NatA/E-HYPK recruited by NAC at the ribosome. The cryo-EM map of the quaternary complex is shown as a solid surface; additional density present only in the map of the quaternary complex with HYPK is shown as a semi-transparent purple difference volume superimposed on the model of the rearranged HYPK.

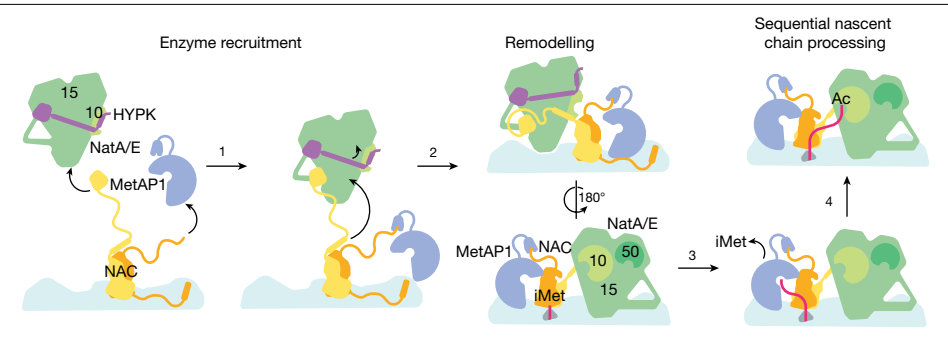


Fig. 5 | Model for ribosome recruitment and activation of NatA and MetAP1 for cotranslational processing of the nascent chain. Step 1, NAC captures NatA/E using the UBA domain of NACα and MetAP1 using the C terminus of NAC $\beta$ . Step 2, the interaction of NAC $\alpha$  H2 with Naa15 positions NatA/E near the exit tunnel and removes the inhibitory contacts from HYPK.

Front (top) and back (bottom) views are shown to depict the protein interactions and positions of the enzyme active sites relative to the exit tunnel. Step 3, MetAP1-mediated iMet excision. Step 4, NatA-mediated N-terminal acetylation of the nascent chain.

bound as previously observed in the RNC-NAC-MetAP1 complex<sup>34</sup>. Together, the multienzyme complex forms a semicircle around the nascent polypeptide exit tunnel, where newly synthesized proteins emerge.

To understand the sequential actions of MetAP1 and NatA, which process the same pool of nascent proteins, we determined the timing of their reactions during translation (Fig. 3c,d). Stalled RNCs with varying nascent chain lengths were translated in RRL. iMet excision by endogenous MetAP1 was measured by the loss of [35S]iMet (Fig. 3c and Extended Data Fig. 1b). The reactions also included fumagillin to prevent iMet excision by MetAP2, which acts redundantly to MetAP1 but independently of NAC34,40. N-terminal acetylation mediated by endogenous NatA was detected using an antibody that specifically recognizes an acetylated N-terminal epitope<sup>37</sup> (Fig. 3d and Extended Data Fig. 1b). We found that iMet excision initiates when the RPL4 nascent chain is at least 60 amino acids long and peaked after about 70 amino acids (Fig. 3c), similar to observations with prokaryotic MetAP<sup>41</sup>. N-terminal acetylation began when the RPL4 nascent chain reached approximately 68 amino acids in length and peaked after around 95 amino acids (Fig. 3d). With the SNAP25 nascent chain, which folds into a rigid helix<sup>42</sup>, the onset of N-terminal acetylation was delayed to over 80 amino acids (Fig. 3d). These results are consistent with the distances of the exit tunnel to the respective enzyme active sites (Fig. 3a) and show that the MetAP1 and NatA reactions are separated by around 25 amino acids during translation elongation, or about 5 s based on a translation elongation rate<sup>43</sup> of 5 amino acids per second.

We next tested whether NAC prepositions both enzymes to facilitate nascent chain handover from MetAP1 to NatA in an in vitro complementation experiment. We generated two mutant NAC heterodimers that are deficient in either NatA recruitment (NAC( $\Delta$ UBA)) or MetAP1 recruitment (deletion of residues 140-162 in the C terminus of NACB or NAC( $\Delta$ C)). We carried out coupled enzymatic reactions that require both iMet excision by MetAP1 and N-terminal acetylation by NatA on a 105-amino-acid-long RNC<sub>RPL4</sub> in the presence of either wild-type NAC, the individual NAC mutants or their equimolar combination (Fig. 3e-g). If the role of NAC is restricted to the ribosome recruitment of both enzymes, the two mutant NAC heterodimers will complement one another and rescue the sequential enzymatic reaction. However, this is not what we observed: the reaction with the combination of NAC mutants was no faster than the reaction with NAC( $\Delta$ C) alone and significantly slower than the reaction with wild-type NAC (Fig. 3g). These results, together with the high-affinity NatA binding to RNC-NAC when the RPL4 nascent chain is around 53 amino acids in length (Fig. 1), suggest that NAC prepositions both enzymes at the ribosome exit tunnel and facilitates handover of the nascent chain to ensure its timely sequential processing.

## NAC activates NatA-HYPK on the ribosome

In higher eukaryotes, NatA activity is regulated by HYPK<sup>5,29,30</sup>, which binds NatA via a C-terminal UBA domain that shares strong sequence homology with the UBA domain of NACα (Fig. 4a). HYPK further sterically blocks and remodels the Naa10 active site via its N-terminal region (Fig. 4a), inhibiting catalytic activity in vitro<sup>5,30</sup>. However, HYPK enhances N-terminal acetylation in three model organisms<sup>4,31,32</sup>, suggesting that an unknown mechanism relieves the inhibitory activity of HYPK in vivo. Using a FRET-based binding assay between HYPK and NatA, we found that the NatA-HYPK complex has ultra-high affinity, with  $K_d \le 150$  pM and a dissociation rate of approximately  $10^{-5}$  s<sup>-1</sup> (Extended Data Fig. 7a-d). The presence of the ribosome or a high-salt wash that contains ribosome-bound proteins did not drive dissociation of NatA-HYPK (Extended Data Fig. 7e). Thus, NatA and HYPK form an obligatory complex, and the de-repression of NatA activity is likely to involve an allosteric mechanism rather than the dissociation of HYPK from NatA.

To test whether and how HYPK and NAC regulate NatA activity on the ribosome, we reconstituted cotranslational N-terminal acetylation reactions using purified protein complexes and RNC bearing the RPL4 nascent chain of 105 amino acids in length (Extended Data Fig. 1c). We recapitulated the inhibitory effect of HYPK on NatA in reactions with the RNC substrate (Fig. 4b, red). When NAC was additionally present, however, N-terminal acetylation by the NatA-HYPK complex occurred with efficiencies that were higher than those observed for NatA alone (Fig. 4b). This reaction was abolished by deletion of the NACα UBA domain or mutation of hydrophobic residues in the NACα UBA domain that contact Naa15 (Fig. 4c), in agreement with the critical role of these contacts in NatA recruitment to the RNC. Thus, NAC relieves the inhibitory effect of HYPK and activates NatA on the ribosome.

Consistent with the biochemical results, knockout of HYPK in C. elegans partially rescued the lethal phenotype in worms in which NAC $\alpha$  was depleted by RNAi (Fig. 4d). Moreover, the N-terminal acetylation defect caused by NACα knockdown was partially reversed in HYPK-knockout worms (Fig. 4d). Therefore, the in vivo function of HYPK is inextricably linked to that of NAC.

We next explored the mechanism underlying the NAC-induced activation of NatA-HYPK. The binding site of NACα UBA on NatA, in the N-terminal helices of Naa15, is distinct from that of HYPK UBA<sup>5</sup>, which binds at the C-terminal TPR region (Fig. 4e,f, top and Extended Data Fig. 8a-d), supporting the notion that NAC and HYPK can bind Naa15 simultaneously. However, structural superposition with the isolated NatA-HYPK structure<sup>5</sup> reveals that NACα H2 would sterically clash with helix H2 of HYPK, which connects its UBA to the N-terminal region that inhibits the Naa10 active site (Extended Data Fig. 8c). Therefore, the

binding to NAC could potentially release the inhibitory N terminus of HYPK from the Naa10 active site while both UBA domains of NAC and HYPK remain anchored to distinct locations on Naa15 (Fig. 4f, bottom).

To test this, we performed single-particle cryo-EM to solve the structure of RNC-NAC-MetAP1 bound to NatA-HYPK (Extended Data Fig. 3 and Supplementary Fig. 2c). The overall configuration of this assembly resembles that of the quaternary complex, with NACa contacting NatA/E through both UBA and H2, which extends from the globular domain of NAC (Fig. 4g and Extended Data Fig. 8e-j). We identified an additional globular density with a tubular extension that, guided by the structure of isolated NatA/E-HYPK, were assigned to the HYPK UBA domain and HYPK H2, respectively (Fig. 4f and Extended Data Fig. 8e-i). The UBA domain of HYPK is positioned as in previous NatA/E-HYPK structures<sup>5,29,30</sup>. However, induced by the steric clash with NACα H2, H2 of HYPK is pushed upwards compared with previous structures, probably leading to derepression of NatA activity. In agreement with these structural observations, the mtNAC(H2) mutant, which retains high-affinity NatA binding to the RNC via UBA contacts (Fig. 2), severely compromised N-terminal acetylation activity (Fig. 4c), demonstrating the importance of NAC $\alpha$  H2 for the remodelling of HYPK and de-inhibition of NatA.

Our study suggests a model of extensive cooperation between NAC, MetAP1 and NatA to ensure the timely and efficient cotranslational N-terminal modification of around 40% of the mammalian proteome (Fig. 5). Given the estimated cellular concentrations of NatA (0.66 μM) and HYPK<sup>44</sup> (0.41 μM), the majority of NatA is tightly bound to HYPK and catalytically inhibited. NAC recruits NatA to the ribosome early during translation using the flexibly tethered UBA domain in NAC $\alpha$ , whereas the C terminus of NAC $\beta$  recruits MetAP1 $^{34}$ . To optimally position their active sites next to the exit tunnel, the two enzymes form additional contacts with NAC and with the ribosome on opposite sides of the NAC globular domain. In NatA, this positioning involves the additional contact of NAC a H2 with NatA and displaces HYPK H2, allowing the release of the inhibitory HYPK N terminus from the active site of Naa10. This leads to catalytic activation of NatA, enabling rapid N-terminal acetylation following iMet excision by MetAP1. The catalytic inhibition of NatA by HYPK off the ribosome and the de-inhibition by NAC on the ribosome further renders this essential modification strictly cotranslational

In addition to the role of NAC in the ribosome recruitment of SRP and MetAP1, recent studies have reported that CHP1, a specialized chaperone that safeguards the cotranslational folding of eEF1A, and potentially PHD2, which mediates the hydroxylation of HIFα during hypoxia response, are both recruited by NAC to the ribosome<sup>33,35,45</sup>. The results here together with these recent findings support a central role of NAC as a molecular interaction hub that controls the access of nascent polypeptide to diverse components of the protein biogenesis machinery at the ribosome exit site. Our data further suggest multiple potential mechanisms of molecular interplay between SRP and nascent protein processing enzymes, including the competition of SRP and NatA for the NAC UBA, steric clashes between MetAP1 and the SRP GTPase domain near the ribosome exit tunnel, and the position of the NAC globular domain that can be regulated by sequence information in the nascent chain. These interplays, which could further modulate the modification efficiency for subsets of the mammalian protein, await investigation.

#### **Online content**

Any methods, additional references, Nature Portfolio reporting summaries, source data, extended data, supplementary information, acknowledgements, peer review information; details of author contributions and competing interests; and statements of data and code availability are available at https://doi.org/10.1038/s41586-024-07846-7.

- Aksnes, H., Drazic, A., Marie, M. & Arnesen, T. First things first: vital protein marks by N-terminal acetyltransferases. *Trends Biochem. Sci* 41, 746–760 (2016).
- Wiedmann, B., Sakai, H., Davis, T. A. & Wiedmann, M. A protein complex required for signal-sequence-specific sorting and translocation. *Nature* 370, 434–440 (1994).
- Gamerdinger, M. et al. Early scanning of nascent polypeptides inside the ribosomal tunnel by NAC. Mol. Cell 75. 996–1006.e8 (2019).
- Arnesen, T. et al. The chaperone-like protein HYPK acts together with NatA in cotranslational N-terminal acetylation and prevention of Huntingtin aggregation. *Mol. Cell. Biol.* 30, 1898–1909 (2010).
- Gottlieb, L. & Marmorstein, R. Structure of human NatA and its regulation by the huntingtin interacting protein HYPK. Structure 26, 925–935.e8 (2018).
- Arnesen, T. et al. Proteomics analyses reveal the evolutionary conservation and divergence of N-terminal acetyltransferases from yeast and humans. Proc. Natl Acad. Sci. USA 106, 8157–8162 (2009).
- Oh, J.-H., Hyun, J.-Y. & Varshavsky, A. Control of Hsp90 chaperone and its clients by N-terminal acetylation and the N-end rule pathway. Proc. Natl Acad. Sci. USA 114, F4370–F4379 (2017).
- Monda, J. K. et al. Structural conservation of distinctive N-terminal acetylation-dependent interactions across a family of mammalian NEDD8 ligation enzymes. Structure 21, 42–53 (2013).
- Scott, D. C. et al. Blocking an N-terminal acetylation-dependent protein interaction inhibits an E3 ligase. Nat. Chem. Biol. 13, 850–857 (2017).
- Behnia, R., Panic, B., Whyte, J. R. C. & Munro, S. Targeting of the Arf-like GTPase Arl3p to the Golgi requires N-terminal acetylation and the membrane protein Sys1p. Nat. Cell Biol. 6 405–413 (2004)
- Hwang, C.-S., Shemorry, A. & Varshavsky, A. N-terminal acetylation of cellular proteins creates specific degradation signals. Science 327, 973–977 (2010).
- Shemorry, A., Hwang, C.-S. & Varshavsky, A. Control of protein quality and stoichiometries by N-terminal acetylation and the N-end rule pathway. Mol. Cell 50, 540–551 (2013).
- Gottlieb, L., Guo, L., Shorter, J. & Marmorstein, R. N-alpha-acetylation of Huntingtin protein increases its propensity to aggregate. J. Biol. Chem. 297, 101363 (2021).
- Vinueza-Gavilanes, R. et al. N-terminal acetylation mutants affect alpha-synuclein stability, protein levels and neuronal toxicity. Neurobiol. Dis. 137, 104781 (2020).
- Kang, L., Janowska, M. K., Moriarty, G. M. & Baum, J. Mechanistic insight into the relationship between N-terminal acetylation of α-synuclein and fibril formation rates by NMR and fluorescence. PLoS ONE 8, e75018 (2013).
- Rope, A. F. et al. Using VAAST to identify an X-linked disorder resulting in lethality in male infants due to N-terminal acetyltransferase deficiency. Am. J. Hum. Genet. 89, 28–43 (2011).
- Bader, I. et al. Severe syndromic ID and skewed X-inactivation in a girl with NAA10 dysfunction and a novel heterozygous de novo NAA10 p.(His16Pro) variant — a case report. BMC Med. Genet. 21, 153 (2020).
- Lee, C.-F. et al. hNaa10p contributes to tumorigenesis by facilitating DNMT1-mediated tumor suppressor gene silencing. J. Clin. Invest. 120, 2920–2930 (2010).
- Kim, S. M. et al. NAA10 as a new prognostic marker for cancer progression. Int. J. Mol. Sci. 21, F8010 (2020).
- Bu, B. et al. N-terminal acetylation preserves α-synuclein from oligomerization by blocking intermolecular hydrogen bonds. ACS Chem. Neurosci. 8, 2145–2151 (2017).
- Lima, V., de, A., do Nascimento, L. A., Eliezer, D. & Follmer, C. Role of Parkinson's disease-linked mutations and N-terminal acetylation on the oligomerization of a-synuclein induced by 3,4-dihydroxyphenylacetaldehyde. ACS Chem. Neurosci. 10, 690–703 (2019).
- Deng, S. & Marmorstein, R. Protein N-terminal acetylation: structural basis, mechanism, versatility, and regulation. *Trends Biochem. Sci.* 46, 15–27 (2021).
- Gautschi, M. et al. The yeast N<sup>a</sup>-acetyltransferase NatA is quantitatively anchored to the ribosome and interacts with nascent polypeptides. *Mol. Cell. Biol.* 23, 7403–7414 (2003)
- Magin, R. S., Deng, S., Zhang, H., Cooperman, B. & Marmorstein, R. Probing the interaction between NatA and the ribosome for co-translational protein acetylation. PLoS ONE 12, e0186278 (2017).
- Varland, S. & Arnesen, T. Investigating the functionality of a ribosome-binding mutant of NAA15 using Saccharomyces cerevisiae. BMC Res. Notes 11, 404 (2018).
- Knorr, A. G. et al. Ribosome-NatA architecture reveals that rRNA expansion segments coordinate N-terminal acetylation. Nat. Struct. Mol. Biol. 26, 35–39 (2019).
- Sandikci, A. et al. Dynamic enzyme docking to the ribosome coordinates N-terminal processing with polypeptide folding. Nat. Struct. Mol. Biol. 20, 843–850 (2013).
- Mullen, J. R. et al. Identification and characterization of genes and mutants for an N-terminal acetyltransferase from yeast. EMBO J. 8, 2067–2075 (1989).
- Deng, S., McTiernan, N., Wei, X., Arnesen, T. & Marmorstein, R. Molecular basis for N-terminal acetylation by human NatE and its modulation by HYPK. Nat. Commun. 11, 818 (2020).
- Weyer, F. A. et al. Structural basis of HypK regulating N-terminal acetylation by the NatA complex. Nat. Commun. 8, 15726 (2017).
- Miklánková, P. et al. HYPK promotes the activity of the N<sup>a</sup>-acetyltransferase A complex to determine proteostasis of nonAc-X2/N-degron-containing proteins. Sci. Adv. 8, eabn6153 (2022).
- Gong, X. et al. OsHYPK-mediated protein N-terminal acetylation coordinates plant development and abiotic stress responses in rice. Mol. Plant 15, 740-754 (2022).
- Jomaa, A. et al. Mechanism of signal sequence handover from NAC to SRP on ribosomes during ER-protein targeting. Science 375, 839–844 (2022).
- Gamerdinger, M. et al. NAC controls cotranslational N-terminal methionine excision in eukaryotes. Science 380, 1238–1243 (2023).
- Song, D., Peng, K., Palmer, B. E. & Lee, F. S. The ribosomal chaperone NACA recruits PHD2 to cotranslationally modify HIF-a. EMBO J. 41, e112059 (2022).
- Hsieh, H.-H., Lee, J. H., Chandrasekar, S. & Shan, S.-O. A ribosome-associated chaperone enables substrate triage in a cotranslational protein targeting complex. *Nat. Commun.* 11, 5840 (2020).

- Connell, E., Darios, F., Peak-Chew, S., Soloviev, M. & Davletov, B. N-terminal acetylation of the neuronal protein SNAP-25 is revealed by the SMI81 monoclonal antibody. Biochemistry 48, 9582-9589 (2009).
- ${\it Jumper, J. et al. Highly accurate protein structure prediction with AlphaFold.}\ {\it Nature~\bf 596,}$ 38. 583-589 (2021).
- Mirdita, M. et al. ColabFold: making protein folding accessible to all. Nat. Methods 19, 39 679-682 (2022).
- 40. Garrabrant, T. et al. Small molecule inhibitors of methionine aminopeptidase type 2 (MetAP-2) fail to inhibit endothelial cell proliferation or formation of microvessels from rat aortic rings in vitro. Angiogenesis 7, 91-96 (2004).
- 41. Yang, C.-l., Hsieh, H.-H. & Shan, S.-O. Timing and specificity of cotranslational nascent protein modification in bacteria. Proc. Natl Acad. Sci. USA 116, 23050-23060 (2019).
- 42. Chen, X. et al. Three-dimensional structure of the complexin/SNARE complex. Neuron 33, 397-409 (2002).
- 43. Ingolia, N. T., Lareau, L. F. & Weissman, J. S. Ribosome profiling of mouse embryonic stem cells reveals the complexity and dynamics of mammalian proteomes. Cell 147, 789-802

- 44. Kulak, N. A., Pichler, G., Paron, I., Nagaraj, N. & Mann, M. Minimal, encapsulated proteomicsample processing applied to copy-number estimation in eukaryotic cells. Nat. Methods 11, 319-324 (2014).
- 45. Minoia, M. et al. Chp1 is a dedicated chaperone at the ribosome that safeguards eEF1A biogenesis. Nat. Commun. 15, 1382 (2024).

Publisher's note Springer Nature remains neutral with regard to jurisdictional claims in published maps and institutional affiliations.

Springer Nature or its licensor (e.g. a society or other partner) holds exclusive rights to this article under a publishing agreement with the author(s) or other rightsholder(s); author self-archiving of the accepted manuscript version of this article is solely governed by the terms of such publishing agreement and applicable law.

© The Author(s), under exclusive licence to Springer Nature Limited 2024

## Methods

### **Protein purification**

HYPK. Human HYPK fused to N-terminal SUMO was expressed from pETm41-SUMO-HYPK. Freshly transformed BL21 (DE3) cells were inoculated in LB medium containing kanamycin (50 μg ml<sup>-1</sup>) and grown at 37 °C to an OD<sub>600</sub> of 0.6, at which time the temperature was lowered to 18 °C and protein expression was induced by 1 mM isopropyl β-D-1-thiogalactopyranoside (IPTG) for 12–16 h. Collected cells were lysed by sonication in lysis buffer (25 mM Tris-HCl pH 8.0, 150 mM NaCl, 10 mM β-mercaptoethanol, 30 mM imidazole) supplemented with ProBlock Gold Protease Inhibitor Cocktail (Goldbio) and 1 mM AEBSF. The lysate was clarified by centrifugation in a JA-20 rotor (Beckman Coulter) at 18.000 rpm for 1 h at 4 °C, followed by incubation with 1 ml pre-equilibrated Ni Sepharose High Performance resin (Cytiva) per 11 of culture for 1 h with rotation at 4 °C. The resin was washed in batch 5 times with 10 column volumes lysis buffer, and the protein was eluted twice with 10 column volumes lysis buffer containing 500 mM imidazole. The N-terminal SUMO tag was cleaved by addition of Ulp1, and the mixture was dialyzed in HYPK Buffer A (25 mM Tris-Cl pH 8.0, 150 mM NaCl, 1 mM TCEP) at 4 °C with rotation overnight. Cleavage was confirmed by SDS-PAGE, and the protein was purified over a MonoQ 10/100 GL anion-exchange column (Cytiva) pre-equilibrated in HYPK buffer A using a 20 column volume linear gradient to 100% HYPK buffer B (50 mM HEPES-KOH pH 7.5, 0.6 M NaCl, 1 mM TCEP, 10% glycerol). Peak fractions were pooled and concentrated to 400-500 µM with a 3 KMWCO centrifugation concentrator (Amicon). Aliquots were frozen in liquid nitrogen and stored at -80 °C. The protein concentration was measured using an extinction coefficient of  $\varepsilon_{280} = 1,490 \, \mathrm{M}^{-1} \, \mathrm{cm}^{-1}$ .

Naa15 and Naa10 (NatA). A URA3 selectable and galactose inducible pRS plasmid co-expressing human 6×His-Naa15 and Naa10 or 6×His-Naa15 and the catalytically impaired Naa10 mutant E24Q/Y26F<sup>46</sup> were used to transform Saccharomyces cerevisiae (strain BCY123). Individual clones were tested for expression and frozen as glycerol stocks at -80 °C. Glycerol stocks were streaked out on uracil (Ura) dropout synthetic defined (SD) agar plates and incubated for 48 h at 30 °C. Five to ten colonies were inoculated into SD-Ura medium supplemented with 2% glucose and grown overnight with shaking at 30 °C. The next morning, a larger-scale SD-Ura medium supplemented with 2% raffinose was inoculated with the overnight culture at a ratio of 1:40 and grown while shaking at 225 rpm at 30 °C to an  $OD_{600}$  of approximately 0.8, at which time protein expression was induced by addition of 2% galactose. After growing overnight, the cells were collected and resuspended in 1 ml lysis buffer (500 mM NaCl, 50 mM potassium phosphate pH7.4, 10% glycerol, 10 mM β-mercaptoethanol, 35 mM imidazole) supplemented with 1 mM AEBSF (Goldbio) and 1× ProBlock Gold Protease Inhibitor Cocktail (Goldbio) per 10 ml cell paste. The resuspension was slowly dripped into liquid nitrogen using a 5-ml serological pipette. The frozen cell kernels were lysed using a pre-cooled CryoMill (Retsch) at 25 Hz for 2 min. The resulting cell powder was thawed with equal volume of lysis buffer until allice crystals disappeared and centrifuged at 42,000 rpm for 45 min at 4 °C in a Type 45 Ti Fixed-Angle rotor (Beckman Coulter). The clarified lysate was then added to 1.5 ml Ni Sepharose High Performance resin (Cytiva) per 1 l of culture and incubated with rotation at 4 °C for 1 h. The resin was washed with 7 column volumes lysis buffer with 1 mM AEBSF in batch for 15 min with rotation, and this step was repeated 4 times. The protein was eluted with 8 column volumes lysis buffer containing 500 mM imidazole and dialyzed overnight into dialysis buffer (20 mM HEPES-KOH pH 7.4, 250 mM NaCl, 5 mM β-mercaptoethanol, 10% glycerol) with 10 K MWCO SnakeSkin (ThermoFisher) dialysis tubing. The dialysed protein was purified over a Mono S 10/100 GL cation exchange column (Cytiva) using a 20 column volume linear gradient from NatA buffer A (20 mM HEPES-KOH pH 7.4, 10% glycerol, 1 mM TCEP, 250 mM NaCl) to 90% NatA buffer B (20 mM HEPES-KOH pH 7.4, 10% glycerol,

1 mM TCEP, 1 M NaCl). Peak fractions were pooled and concentrated using a 50 K MWCO centrifugation concentrator (Amicon), and aliquots were frozen in liquid nitrogen. The protein concentration was measured using an extinction coefficient of  $\varepsilon_{280} = 132,480 \, \text{M}^{-1} \, \text{cm}^{-1}$ .

**Naa50.** Human Naa50 carrying an N-terminal GST tag was expressed from pGEM-GST-hNaa50 (a gift from the Marmorstein laboratory) and purified according to the protocol in ref. 5, except for omitting the final gel filtration chromatography step. The protein concentration was determined using an extinction coefficient of  $\varepsilon_{280}$  = 13,410 M<sup>-1</sup> cm<sup>-1</sup>.

**NAC.** The human NAC heterodimer consisting of NAC $\alpha$  with an N-terminal 6×His tag and NACβ was expressed from a pET28b-NAC plasmid, Freshly transformed BL21 (DE3) cells were grown in LB medium containing kanamycin (50 μg ml<sup>-1</sup>) to an OD<sub>600</sub> of 0.6, at which time temperature was lowered to 18 °C, and protein expression was induced by addition of 1 mM IPTG for 12-16 h. Cells were lysed by sonication in NAC lysis buffer (50 mM HEPES-KOH pH 7.5, 1 M NaCl, 6 mM β-mercaptoethanol, 30 mM imidazole, 10% glycerol) supplemented with 1× ProBlock Gold Protease Inhibitor Cocktail (Goldbio) and 1 mM AEBSF and clarified by centrifugation in a JA-20 rotor (Beckman Coulter) in an Avanti J-E centrifuge (Beckman Coulter) at 18,000 rpm for 1 h. The clarified lysate was incubated with 1 ml of Ni Sepharose High Performance resin (Cytiva) per 1 l of culture for 1 h with rotation at 4 °C. The resin was washed in batch with 50 column volumes of NAC lysis buffer and eluted twice with 5 column volumes of NAC elution buffer (50 mM HEPES-KOH pH 7.5, 100 mM NaCl, 500 mM imidazole, 1 mM TCEP, 10% glycerol). The N-terminal 6xHis tag was cleaved using PreScission Protease with rotation overnight at 4 °C. The protein was purified over a Mono Q10/100 GL anion-exchange column (Cytiva) pre-equilibrated in NAC Buffer A (50 mM HEPES-KOH pH 7.5, 100 mM NaCl, 1 mM TCEP, 10% glycerol) and eluted with a 10 column volume linear gradient to 50% NAC Buffer B (50 mM HEPES-KOH pH 7.5, 1 M NaCl, 1 mM TCEP, 10%glycerol). Peak fractions were pooled concentrated with a 3 K MWCO centrifugation concentrator (Amicon). Aliquots were frozen in liquid nitrogen and stored at -80 °C. The protein concentration was measured using an extinction coefficient of  $\varepsilon_{280} = 2,980 \,\mathrm{M}^{-1}\,\mathrm{cm}^{-1}$ .

SFP. SFP was purified according to a previously established protocol with modifications<sup>47</sup>. In brief, SFP with a PreScission Protease-cleavable C-terminal 6xHis tag was expressed from pET29 Sfp-Pre-His, Freshly transformed BL21 (DE3) cells were grown in LB medium containing kanamycin (50  $\mu g$  ml<sup>-1</sup>) at 37 °C to an OD<sub>600</sub> of 0.6, at which point protein expression was induced by addition of 1 mM IPTG. The culture was grown at 25 °C for 6 h and at 15 °C overnight. Clarified lysate in SFP Buffer (20 mM Tris-HCl pH 8.0, 500 mM NaCl, 5 mM imidazole) supplemented with 1× ProBlock Gold Protease Inhibitor Cocktail (Goldbio) was incubated with 2 ml pre-equilibrated Nickel NTA agarose resin (Goldbio) for 1 h with rotation at 4 °C. The resin was washed in gravity flow with 50 column volumes SFP Buffer, and the tagged protein was eluted with 7.5 ml elution buffer (50 mM Tris-HCl pH 7.0, 125 mM NaCl, 1 mM EDTA, 1 mM DTT, 500 mM imidazole). The eluted protein was incubated with PreScission Protease at 4 °C with rotation overnight and purified over a MonoQ10/100 GL anion-exchange column (Cytiva) using a gradient of 125-500 mM NaCl over 20 column volumes. Peak fractions were dialysed into SFP storage buffer (10 mM Tris-HCl pH 7.4, 1 mM EDTA, 10% glycerol), and aliquots were frozen in liquid nitrogen and stored at -80 °C.

MetAP1. MetAP1 and the catalytically impaired MetAP1 D220N mutant<sup>34</sup> were purified essentially as previously described<sup>34</sup>. In brief, human MetAP1 was expressed as a His-SUMO fusion protein in *Escherichia coli* BL21(DE3) cells. After His affinity purification using a Talon cobalt resin (Takara), the His-SUMO tag was cleaved by SUMO protease (Ulp1) and MetAP1 purified by ion exchange chromatography. After

dialysis overnight into storage buffer (20 mM Na-PO $_4$  pH 7.4, 25 mM NaCl, 6 mM MgCl $_2$ , 5% glycerol), the protein was frozen in liquid N $_2$ , and stored at  $-80\,^{\circ}$ C.

#### **RNC** purification

In vitro transcription of mRNA. Templates for in vitro transcription were generated by PCR, resulting in amplicons that included a T7 promoter at the 5' end followed by an IRES sequence and the protein of interest lacking a stop codon at the 3' end. Amplicons were purified using a Qiagen PCR purification kit. Transcription was performed for 4 h at 37 °C with 5 ng  $\mu l^{-1}$  DNA template, 7.5 mM of each NTP, 40 mM Tris-HCl pH 8.0, 10 mM DTT, 2 mM spermidine (Sigma), 20 mM MgCl $_2$ , 0.015 U  $\mu l^{-1}E$ . coli inorganic pyrophosphatase (NEB), 0.4 U  $\mu l^{-1}$ RNase inhibitor (Ambion), and homemade T7 RNA polymerase. Transcription reactions were cleaned up by LiCl precipitation, and the pellets were resuspended in ddH $_2$ O and stored at -80 °C.

Generation and purification of RNC. In vitro translation was performed in RRL according to established protocols<sup>48</sup>. In brief, the translation reaction was performed for 30 min at 32 °C with 1×T2 mix containing the RRL, amino acids, and an energy mix (see ref. 48 for details), 1.5 mM MgCl<sub>2</sub>, 50 mM KCl, 0.3 mM spermidine (Sigma), 5 mM DTT, and 40 µM methionine. After in vitro translation, the reaction was supplemented to 15 mM magnesium acetate, 666 mM potassium acetate, and 0.1% Triton X-100 (Sigma) and layered over a high-salt sucrose cushion (50 mM HEPES-KOH pH 7.5, 1 M potassium acetate, 15 mM magnesium acetate, 0.5 M sucrose, 0.1% Triton X-100), followed by centrifugation in a TLA100.3 rotor (Beckman Coulter) at 100,000 rpm for 1 h at 4 °C. The pellets were resuspended with Resuspension Buffer (50 mM HEPES-KOH pH 7.5, 100 mM potassium acetate, 2 mM magnesium acetate), and the resuspension was centrifuged at 14,000g for 10 min to remove large aggregates. RNCs with an N-terminal 3×Flag-SUMO tag were incubated with anti-DYKDDDDK magnetic agarose resin (Pierce A36797) for 1 h with rotation at 4 °C. Beads were washed 3 times with 3 column volumes wash buffer 1 (50 mM HEPES-KOH pH 7.5, 300 mM potassium acetate, 2 mM magnesium acetate), 3 times with 3 column volume wash buffer 2 (50 mM HEPES-KOH pH 7.5, 100 mM potassium acetate, 2 mM magnesium acetate, 0.1% Triton-X100), and once in 5 column volumes of resuspension buffer. RNCs were eluted with 2 column volumes of elution buffer (50 mM HEPES-KOH pH 7.5, 100 mM potassium acetate. 2 mM magnesium acetate. 1.5 mg ml<sup>-1</sup> 3×Flag peptide (Apex Bio. SKU: A6001-25)), and the tag was cleaved from the nascent chain using 1 µM Ulp1 SUMO protease (homemade) for 1 h at 4 °C. After cleavage, the RNCs were centrifuged through a 0.5 M sucrose cushion in SRP buffer (50 mM HEPES-KOH pH 7.5, 150 mM potassium acetate, 5 mM magnesium acetate) in a TLA 120.2 rotor (Beckman Coulter) at 100,000 rpm for 1 h at 4 °C. The resulting pellet was resuspended in SRP buffer (50 mM HEPES-KOH pH 7.5, 150 mM potassium acetate, 5 mM magnesium acetate, 1 mM fresh DTT, 0.02% octaethylene glycol monododecyl ether (Sigma)). RNCs were flash-frozen in liquid nitrogen and stored at -80 °C in single-use aliquots.

#### Fluorescence labelling

Cysteine-maleimide labelling of NAC and HYPK. Cys-less NAC and HYPK were engineered to harbor a single cysteine (NAC $\alpha$ (S186C), NAC $\beta$ (A57C) and HYPK(T92C)) and purified as the wild-type protein. Single-cysteine mutants were labelled in labelling buffer (50 mM HEPES-KOH pH 7.5, 100 mM NaCl, 1 mM TCEP, and 20% glycerol) with a fivefold molar excess of maleimide-conjugated dye (BODIPY-FL (BDP), maleimide (Invitrogen B10250), or tetramethylrhodamine-5-maleimide (TMR) single isomer (Invitrogen T6027)). Not incorporated dye was removed with a homemade 40 ml Sephadex G25 fine column (GE Healthcare). Peak fractions were pooled and concentrated with a 10 K MWCO centrifugation filter (Amicon), and aliquots were frozen and stored at  $-80\,^{\circ}\text{C}$ .

ybbR-SFP labelling of NatA. Coenzyme A (CoA) conjugates of TMR were generated by reacting maleimide-conjugated dve with a 1.75 molar excess of CoASH in 0.25 ml DMSO and 0.75 ml 100 mM Na•Phosphate pH 7.0 while stirring in the dark for 1 h at room temperature. The reaction was purified by HPLC chromatography using a C18 wide pore column (Supelco Analytical) with a 0-100% acetonitrile gradient. Peak fractions were lyophilized for approximately 36 h, and purified CoA-dye conjugate was resuspended in DMSO. The 11-residue ybbR tag<sup>47,49</sup> was appended to the N terminus or inserted at residue 651 of Naa15. ybbR-tagged proteins were purified similar to wild-type proteins and labelled in SFP labelling buffer (50 mM HEPES-KOH pH 7.5.150 mM NaCl, 10 mM MgCl<sub>2</sub>) with stoichiometric amounts of SFP enzyme and a 2.5 molar excess of CoA-dye conjugate for 1 h in the dark at room temperature. Free dye and SFP were removed using Ni-HP resin. Labelled NatA was exchanged into storage buffer (25 mM HEPES-KOH pH 7.5, 200 mM NaCl, 1 mM TCEP, 20% glycerol) using a PD10 column (Cytiva), concentrated using an Amicon centrifugation concentrator, flash frozen in aliquots in liquid nitrogen, and stored at -80 °C.

**RNC** labelling. RNC bearing the N-terminal 53 amino acids of the RPL4 nascent chain (RNC  $_{\text{RPL4-53aa}}$ ) was labelled with BODIPY-FL (BDP) at residue 12. To generate fluorescent RNCs, an amber codon was incorporated into the mRNA, and an amber suppressor system was used to insert the noncanonical amino acid TCOK, which reacts with tetrazine-conjugated BODIPY-FL (see ref. 36 for details on the optimization of the amber suppression system). Labelled RNCs were purified as described for unlabelled RNC.

# Preparation of high-salt wash fractions of RNC-protein complexes

The high-salt wash fraction of ribosome-bound cofactors were purified from RRL according to previously established protocols<sup>36</sup>.

#### Biochemical measurements in extract

**MetAP1 reaction in RRL.** Amplicons of different sizes were generated by PCR and in vitro transcribed to generate mRNAs encoding the N-terminal 40, 45, 50, 60, 70, 80 and 100 residues of the RPL4 nascent chain with a single iMet. A negative control, which encodes a tryptophan at position 2 representing a poor MetAP1 substrate  $^{50}$ , was translated in parallel. mRNAs were translated in RRL as described in the RNC purification section, except that RRL was pretreated with MNase (homemade), supplemented with 0.1  $\mu$ M fumagillin, and that 4  $\mu$ M of unlabelled Met and 0.25  $\mu$ Ci  $\mu$ l $^{-1}$ [ $^{35}$ S]Met was used. Reaction products were layered over a high-salt sucrose cushion (50 mM HEPES-KOH pH 7.5, 1 M potassium acetate, 15 mM magnesium acetate, 0.5 M sucrose, 0.1% Triton X-100) and centrifuged in a TLA100 rotor (Beckman Coulter) at 100,000 rpm for 1 h at 4 °C. A radioactive loading control consisting of Skd3–Ank fusion protein translated by the PURE system was added prior to loading onto the gel.

The PURE system (NEB) was used to generate Skd3–eGFP fusion protein as a loading control. 12.5  $\mu$ l PURE-IVT reactions containing 5  $\mu$ l solution A, 3.75  $\mu$ l solution B, 1.6 U  $\mu$ l<sup>-1</sup>RNase I (Ambion), 12 ng  $\mu$ l<sup>-1</sup> of the Skd3–eGFP fusion protein plasmid, 1.48  $\mu$ Ci  $\mu$ l<sup>-1</sup>[ $^{35}$ S]Met were incubated for 2 h at 37 °C. The reaction was diluted 1:16, and 2  $\mu$ l was added to each extract reaction prior to loading the entire reaction onto a 4–12% Bis–Tris gel (Genscript) using low pH loading dye. Gels were imaged using autoradiography, and the resulting bands were quantified using ImageJ v1.53t.

**NatA reaction in RRL.** Amplicons of different sizes were generated by PCR and in vitro transcribed to generate mRNAs encoding SNAP25 nascent chain of 20, 60, 70, 84, 97, 111, 120 and 130 amino acids in length or RPL4 nascent chains of 45, 68, 88, 95, 105 and 115 amino acids in length, which include the 11-residue N-terminal SMI epitope derived from SNAP25. N-terminal acetylation was detected using the SMI81

monoclonal antibody. A negative control, which encodes a proline at position 2, a substrate that cannot be acetylated  $^{\rm l}$ , was translated in parallel. mRNAs were translated in RRL as described in the RNC purification section in 125-µl reactions. The reactions were layered over a 125 µl high salt sucrose cushion and centrifuged in a TLA 100 rotor (Beckman Coulter) for 1 h at 100,000 rpm and resuspended in 20 µl equilibrium buffer. One-hundred nanomolar RNC in 10 µl was loaded onto a 4–12% Bis—Tris gel and imaged by immunodetection. The immunoblots were blocked for 1 h with 3% BSA in PBS-T, and then probed simultaneously with primary antibodies for RPL10 and SMI81. The blots were probed for 45 min with the secondary antibodies, and bands were quantified using Imagel v1.53t.

# Biochemical measurements using purified proteins and complexes

Prior to all assays, proteins were centrifuged for 30 min at 4 °C at 100,000 rpm in a TLA 100 rotor (Beckman Coulter) in an Optima TLX Ultracentrifuge (Beckman Coulter). RNCs were centrifuged for 5 min at 4 °C at 10,000 rpm in a 5425 rotor (Beckman Coulter).

N-terminal acetylation reactions on peptide substrates. Reactions were carried out using a previously described protocol<sup>51</sup> with minor variations. Reactions contained various concentrations of H4 peptide substrate (sequence SGRGKGGKGLGKGGAKRHR, Genscript), 80 μM acetyl-coenzyme A (acetyl-CoA) (Sigma), 20 μM [14C] acetyl-CoA (60 mCi mmol<sup>-1</sup>), 10 nM human NatA (hNatA) in reaction buffer containing 100 mM HEPES-KOH pH 8.0, 50 mM NaCl, 2 mg ml<sup>-1</sup> bovine serum albumin (BSA), 5 mM DTT, and 0.02% octaethylene glycol monododecyl ether (Sigma). NatA was preincubated with H4 peptide at room temperature for 2 min, and the reaction was initiated by adding an equal volume of a 2× acetyl-CoA mixture for a final reaction volume of 125 µl. The reaction was stopped at various time points in the linear range by blotting 20 µl onto a 1.5 cm<sup>2</sup> P81 phosphocellulose paper (J. Oakhill) and immediately placing it into wash buffer (20 mM HEPES-KOH pH 7.4). Unincorporated [14C] acetyl-CoA was removed with 3×15 ml 5-min washes, and the paper squares were air-dried for 2 h. The paper squares were then added to large scintillation vials with 15 ml of safety-solve scintillation fluid (Research products international), vortexed for 3 min, and incubated overnight. Scintillation counts were measured by a scintillation system (Beckman Coulter LS6500) with an integration time of 5 min. The substrate concentration dependence of initial velocities was fit to the Michaelis-Menten equation to obtain the turnover number  $(k_{cat})$  and Michaelis constant ( $K_m$ ).

Reconstituted RNC acetylation assay. RNCs were generated in which the nascent chain contains an N-terminal SUMO, followed by residues 2-12 of SNAP25 and residues 1-94 of RPL4. The N-terminally acetylated 11 residues of SNAP25 are specifically recognized by the SMI81 antibody<sup>37</sup>, providing a readout for N-terminal acetylation on the RNC after the cleavage of SUMO by Ulp1. Reactions were carried out in RNC buffer (50 mM HEPES-KOH pH 7.5, 150 mM potassium acetate, 5 mM magnesium acetate, 5 mM DTT, and 0.02% octaethylene glycol monododecyl ether (Sigma)) and contained 70 nM RNC  $_{\text{SNAP25-RPL4}}$  , 100  $\mu\text{M}$  acetyl-CoA (Sigma), 10 nM hNatA or hNatA-HYPK complex (formed with 1:1.2 molar ratio), and 200 nM NAC where indicated. Reactions were initiated by addition of acetyl-CoA. Reaction aliquots were removed at 10, 20, 30 and 50 s and quenched in 4× low pH loading dye (30% glycerol, 250 mM Bis-Tris, pH 5.7, 0.04% bromophenol blue, 8% SDS, 200 mM DTT) and flash freezing in liquid nitrogen. Reactions were analysed by SDS-PAGE on 4-12% Bis-Tris gels run at 100 V to avoid hydrolysis of the covalent nascent chain-tRNA bond, followed by western blot using primary antibodies for RPL10 (1:2,000, Abcepta, AP19053a) and SMI81 (1:2,000 BioLegend, 836304). The blots were probed for 45 min with the secondary antibodies Goat anti-Rabbit (1:20,000 Licor, IRDye 680RD) and Goat anti-Mouse (1:15,000 Licor, IRDye 800CW). Bands were quantified using ImageJ v1.53t.

Coupled iMet excision and N-terminal acetylation reactions on the RNC were carried out similarly using an RNC bearing a 105-amino-acid-long RPL4 nascent chain with iMet. Reactions were carried out in RNC $_{200}$  buffer (50 mM HEPES-KOH pH 7.5, 200 mM potassium acetate, 5 mM magnesium acetate, 2 mM TCEP, 100  $\mu$ M CoCl $_2$ , and 0.02% octaethylene glycol monododecyl ether (Sigma)) and contained 100 nM RNC, 200 nM of the indicated NAC variant, 5 nM NatA+HYPK. Reactions were initiated with an equal volume of 100  $\mu$ M Acetyl-CoA and 5 nM MetAP1 (final concentrations). 10  $\mu$ l of the reaction was quenched at 20, 30 and 60 s with 4× low pH SDS-loading buffer and analysed as above.

Fluorescence emission spectra. All fluorescence measurements were carried out on a Fluorolog 3-22 or FluoroQM-75-22 spectrofluorometer (HORIBA) at 25 °C in RNC buffer with 1 mg ml<sup>-1</sup>BSA. Data were collected using FelixFL v1.0.34.0 (HORIBA). Fluorescence spectra were recorded using an excitation wavelength of 485 nm and emission wavelengths from 500-600 nm. FRET between BODIPY-FL-labelled RNC<sub>RPL4</sub> (RNC<sup>BDP</sup>) and TMR-labelled at N-terminally ybbR-tagged Naa15-Naa10(E24Q/ Y26F) (NatA<sup>TMR</sup>) was detected using samples containing 1 nM RNC<sup>BDP</sup>, 100 nM NatA<sup>TMR</sup>, and/or 1 µM unlabelled NatA where indicated. FRET between BODIPY-FL-labelled ybbR-Naa15-Naa10(E24Q/Y26F)  $(NatA^{BDP})$  and TMR-labelled  $NAC\alpha(S186C)$ -NACB  $(NAC^{TMR})$  was detected using samples containing 5 nM NAC<sup>TMR</sup>, 5 nM NatA<sup>BDP</sup>, 5 nM unlabelled NAC(S186C), and 5 nM RNC bearing the N-terminal 53 amino acids of RPL4 where indicated. FRET between NatA labelled with BODIPY-FL in ybbR inserted at residue 651 of Naa15 (NatABDP) and HYPK labelled with TMR at C92 (HYPK<sup>TMR</sup>) was detected using 5 nM NatA<sup>BDP</sup> with and without 50 nM HYPK<sup>TMR</sup>.

**Equilibrium titrations.** To measure the binding affinity between RNC<sup>BDP</sup> and NatA<sup>TMR</sup>, equilibrium titrations were performed in RNC buffer using 1 nM RNC<sup>BDP</sup> or preformed RNC<sup>BDP</sup>–NAC complex and indicated concentrations of NatA<sup>TMR</sup>. Fluorescence emission of RNC<sup>BDP</sup> was recorded using an excitation wavelength of 485 nm and emission wavelength of 517 nm. A control titration with unlabelled NatA was carried out in parallel. Raw fluorescence intensities were corrected for dilution and buffer background, and FRET efficiencies (*E*) were calculated using equation (1):

$$E = 1 - \frac{F_{\text{DA}}}{F_{\text{D}}} \tag{1}$$

in which  $F_{DA}$  and  $F_{D}$  are the donor fluorescence intensities in the titrations with NatA<sup>TMR</sup> and unlabelled NatA, respectively. The NatA concentration dependence of E was fitted <sup>52</sup> to equation (2):

$$E = E_{\text{max}} \times \frac{K_{\text{d}} + [A]_0 + [T] - \sqrt{(K_{\text{d}} + [A]_0 + [T])^2 - 4[A]_0[T]}}{2[A]_0}$$
(2)

in which [A] $_0$  and [T] are the total concentrations of analyte (RNC) and titrant (NatA), respectively,  $E_{\rm max}$  is the FRET efficiency at saturating titrant concentrations, and  $K_{\rm d}$  is the equilibrium dissociation constant.  $K_{\rm d}$  was constrained to be greater than 0.1 nM during fitting. Data fitting was performed using Prism v10.1.0.

To measure the  $K_{\rm d}$  between NatA and HYPK, increasing concentrations of HYPK<sup>TMR</sup> were incubated with 5 nM NatA labelled with BODIPY-FL at 651. Donor fluorescence emission of individual reactions were recorded on the SpectraMax iD5 plate reader (Molecular devices) with opaque 96-well plates using an excitation wavelength of 485 nm and an emission wavelength of 525 nm. Data were fit to equation (2). To measure the effect of the ribosome on the NatA–HYPK complex, a complex pre-formed with 10 nM NatA<sup>BDP</sup> and 50 nM HYPK<sup>TMR</sup> was

incubated with increasing concentrations of 80 S. Fluorescence was recorded using the plate reader as described above.

**Dissociation rate constant measurements.** A preformed complex with 5 nM NatA  $^{\text{BDP}}$  and 100 nM HYPK  $^{\text{TMR}}$  was chased with 2  $\mu$ M unlabelled HYPK in RNC buffer. The time course of fluorescence change was recorded on the plate reader as described above. The data were fit to a single exponential equation.

#### Assembly of macromolecular complexes for cryo-EM studies

All complexes were assembled in cryo-EM buffer (50 mM HEPES-KOH pH 7.4, 100 mM potassium acetate, 5 mM magnesium acetate, 0.02% octaethylene glycol monododecyl ether). For the RNC  $_{\text{RPL4}}$ –NAC–NatA/E complex, RNC  $_{\text{RPL4}}$  and NAC were mixed at final concentrations of 80 nM and 500 nM, respectively. The mixture was incubated for 10 min at room temperature, then mixed with the catalytically impaired NatA (Naa10(E24Q/Y26F)) and Naa50 at final concentrations of 1  $\mu$ M, incubated at room temperature for 10 min and then placed on ice until grid preparation. The RNC  $_{\text{RPL4}}$ –NAC–MetAP1–NatA/E complex was prepared similarly, except for the additional presence of 1  $\mu$ M catalytically impaired MetAP1 (D220N mutant) in the final incubation step. For the RNC  $_{\text{RPL4}}$ –NAC–MetAP1–NatA/E complex prepared as above was further mixed with HYPK at a final concentration of 2  $\mu$ M, incubated at room temperature for 10 min and then placed on ice until grid preparation.

#### Cryo-EM grid preparation and data collection

For cryo-EM sample preparation, Quantifoil R2/2 Cu 300 grids were washed with ethyl acetate, coated with a 1 nm thick continuous layer of amorphous carbon (produced in-house) and glow-discharged for 15 s at 15 mA using PELCO easiGlow glow discharge cleaning system (Ted Pella). Grids were mounted into Vitrobot MK IV (Thermo Fisher Scientific) with the chamber set to 4 °C and 95% humidity. Four microlitres of sample were applied to a grid and the sample was incubated for 30 s in the Vitrobot chamber, excess sample was blotted off grids for 2–4 s with a blot force of 15, and grids were plunge-frozen in a mixture of ethane and propane (1:2).

Grids were imaged in a Titan Krios G3i (RNC  $_{RPL4}$ -NAC-NatA/E and RNC  $_{RPL4}$ -NAC-MetAP1-NatA/E-HYPK samples) or Titan Krios G4 (RNC  $_{RPL4}$ -NAC-MetAP1-NatA/E) transmission electron microscope operating at 300 kV and equipped with a BioQuantum (Krios G3i) imaging filter or a BioContinuum (Krios G4) imaging filter-mounted K3 direct electron detector, operating in 2× binned super-resolution mode. The microscope was used with a nominal magnification of 81,000×. The energy filter slit was set to 20 e  $^-$ V, the defocus was set to shift between -0.6 and  $-2.4~\mu m$  in 0.3- $\mu m$  steps.

Automated data collection was set up in EPU software (Thermo Fisher Scientific). For the RNC<sub>RPL4</sub>-NAC-NatA/E sample, a total of 8,739 movies were collected at a physical pixel size of 1.06 Å per pixel with the total electron dose of 60 e $^{-}$ Å $^{-2}$  using EPU 2.10.0.5; for the RNC<sub>RPL4</sub>-NAC-MetAP1-NatA/E sample, a total of 8,888 movies were collected at a physical pixel size of 1.065 Å per pixel with the total electron dose of 50 e $^{-}$ Å $^{-2}$  using EPU 3.0.0.4164; for the quaternary HYPK complex, a total of 9,330 movies were collected at a physical pixel size of 1.06 Å per pixel with the total electron dose of 50 e $^{-}$ Å $^{-2}$  using EPU 3.2.0.4776.

#### **Cryo-EM data processing**

RNC<sub>RPL4</sub>-NAC-NatA/E sample (ternary complex). Movie frames were motion-corrected, dose-weighted and summed into micrographs using CryoSPARC Live. Particles were picked with blob picker (circular blob, 250–350 Å blob diameter range) in CryoSPARC Live. Picked particles were extracted with a box size of 560 pixels and binned 3 times to a box size of 186 pixels. Picked particles were subjected to 2D classification (number of classes set to 200) in CryoSPARC, and 457,759 particles from 2D classes were selected for further processing.

Following a homogeneous refinement in CryoSPARC, particles were further subjected to 3D classification in Relion 3.1 (ref. 53) to first select translating ribosomes with a P-site tRNA (239,646 particles, 52% of all ribosomes; non-default 3D classification parameters are listed in Supplementary Fig. 2a) and then out of those the RNCs with NAC and NatA/E bound (mask used in the 3D classification covered NAC and NatA/E; non-default parameters are listed in Supplementary Fig. 2a). The identified 37,434 particles with well-defined NAC-NatA/E (8% of all ribosome particles) were reimported into CryoSPARC<sup>54</sup>, reextracted without binning, and used for a homogeneous refinement (non-default parameters are listed in Supplementary Fig. 2a) resulting in a map of RNC<sub>RPI.4</sub>-NAC-NatA/E complex to an overall resolution of 2.9 Å, estimated using the Fourier shell correlation (FSC) = 0.143 criterion<sup>55</sup>. The map was then further locally refined (non-default parameters are listed in Supplementary Fig. 2a) first with a mask covering both NAC and NatA/E, and then with a mask covering only the core of NatA/E (non-default parameters are listed in Supplementary Fig. 2a), to an overall resolution of 6.5 Å (Extended Data Table 1).

80S-NAC-NatA/E sample. As we saw NAC-NatA/E bound to ribosomes regardless of the translation state, we opted to pool ribosome particles with these factors regardless of whether they contain a nascent chain or not and performed 3D classifications on NatA/E using CryoSPARC in order to improve the resolution of the NAC-NatA/E segment of the map. First, 197,483 ribosomes with NatA/E (43% of all ribosome particles) were selected through focused 3D classification on the binned data. Selected particles were then reextracted without binning and homogeneously refined (Supplementary Fig. 3). Particles homogeneous with respect to NAC-NatA/E conformation were then selected by performing 3D classification with a focused mask covering the core of NatA/E (non-default parameters are listed in Supplementary Fig. 3). 20,439 particles (4.5% of all ribosome particles) of the 3D class showing finer features of NatA/E structure were used to reconstruct a map with an overall resolution of 3.21 Å (Supplementary Fig. 3b), and the resolution of the NAC-NatA/E segment of 4.52 Å (Supplementary Fig. 3c), estimated using the FSC = 0.143 criterion. FSC for the NAC-NatA/E segment of the map was calculated with a mask on the respective part of the map.

#### RNC<sub>RPI 4</sub>-NAC-MetAP1-NatA/E sample (quarternary complex).

Movie frames were motion-corrected, dose-weighted, and summed into micrographs using CryoSPARC Live. Particles were picked with blob picker (circular blob, 250-350 Å blob diameter) in CryoSPARC Live. Picked particles were extracted with a box size of 560 pixels and binned 3 times to a box size of 186 pixels. Picked particles were subjected to 2D classification (number of classes set to 200) in CryoSPARC, and 360,184 particles from 2D classes were selected for further processing. Following a homogeneous refinement, particles were further classified in parallel for presence of NAC-NatA/E (3D classification with mask covering NAC and NatA/E, non-default parameters are listed in Supplementary Fig. 2b) and NAC-MetAP1 (3D classification with mask covering NAC and MetAP1, non-default parameters are listed in Supplementary Fig. 2b) and for the functional state of ribosomes (3D variability analysis, non-default parameters are listed in Supplementary Fig. 2b). Subsets of particles corresponding to ribosome-NAC-NatA/E or ribosome-NAC-MetAP1 complexes were intersected to arrive at a particle stack for the ribosome-NAC-MetAP1-NatA/E complex. The resulting particle set was then intersected with the RNC subset identified in a parallel branch of classification to yield particles corresponding to an RNC-NAC-MetAP1-NatA/E complex. The map of the RNC-NAC-MetAP1-NatA/E complex was reconstructed from selected 21,864 particles (6% of all ribosomes) and refined with particles re-extracted without binning to an overall resolution of 3.7 Å. The map was then locally refined with a mask, covering NatA/E-NAC-MetAP1 to an overall resolution of 6.7 Å.

RNC<sub>PDI 4</sub>-NAC-(MetAP1)-NatA/E-HYPK sample. Movie frames were motion-corrected, dose-weighted, and summed into micrographs using CryoSPARC Live. Particles were picked with blob picker (circular blob, 250–350 Å blob diameter) in CryoSPARC Live. Picked particles were extracted with a box size of 560 pixels and binned 3 times to a box size of 186 pixels. Picked particles were subjected to two rounds of 2D classification (first with the number of classes set to 200, then to 50) in CryoSPARC, and 156,452 particles were selected for further processing. Following a homogeneous refinement, particles were further classified in parallel for the presence of NAC-NatA/E (3D classification with mask covering NAC and NatA/E, non-default parameters are listed in Supplementary Fig. 2c) and for the functional state of ribosomes (3D) variability analysis, non-default parameters are listed in Supplementary Fig. 2c). Subsets of particles corresponding to ribosome-NAC-NatA/E and RNCs were intersected to arrive at a set of 23,034 particles (15% of all ribosomes) for the RNC-NAC-(MetAP1)-NatA/E-HYPK complex (the parentheses around MetAP1 denote that as we did not exclude ribosomes without MetAP1 bound during 3D classification, the MetAP1 cryo-EM density appears fragmentary due to partial occupancy). The map of the RNC-NAC-(MetAP1)-NatA/E-HYPK complex was reconstructed from selected particles, which were then re-extracted without binning to refine the map to an overall resolution of 3.2 Å. The map was then locally refined with a mask, covering NatA/E-NAC-MetAP1 to an overall resolution of 5.8 Å. To generate a difference volume between locally refined maps of the quaternary complex and the RNC-NAC-(MetAP1)-NatA/E-HYPK, both maps were aligned in ChimeraX<sup>56</sup>, then the former was subtracted from the latter. The resulting volume was multiplied by the mask used previously for refinement of both maps.

AlphaFold prediction of Naa15–NAC $\alpha$  complex structure. Structure prediction of the human Naa15–NAC $\alpha$  complex was done with the ColabFold 1.3 (ref. 39) implementation of AlphaFold2-multimer-v2 (ref. 38) using default parameters. Amino acid sequences of Naa15 (sequence id Q9BXJ9-1) and NAC $\alpha$  (Q13765-1) were retrieved from the UniProt database.

Model building and refinement. Models of ribosomal subunits (from PDB 8P2K), NAC heterodimer (from PDB 7QWR), NatA and Naa50 (PDB 6PPL), HYPK (from PDB 6PW9) and MetAP1 (PDB 2B3H) were docked as rigid groups into respective cryo-EM density maps. In the model of the small ribosomal subunit, the P-site tRNA was remodelled with N residues except for the CCA motif, a mRNA triplet of N residues was built, and the E-site tRNA removed. In the model of the large ribosomal subunit, the nascent polypeptide within the ribosome exit tunnel was built as a poly-UNK chain. The N-terminal segment (amino acid residues 5–112) and the previously unresolved internal basic helix with adjacent linkers (residues 574-637) of Naa15 were transplanted from the AlphaFold<sup>38,39</sup> model of the Naa15-NACα complex. NACα H2 (residues 135–145) and UBA domain (residues 178–215) were transplanted from the AlphaFold model of the Naa15-NACα complex. The docked models were manually adjusted in Coot<sup>57</sup> to better fit the EM maps and then refined using Phenix<sup>58</sup>. First, the RNC models were real-space refined into homogenously refined EM maps for 5 macrocycles including coordinate and ADP refinement with enabled secondary structure restraints. The NAC, MetAP1 and NatA/E-HYPK models were first real-space refined into the better resolved locally refined EM maps using similar settings. The resulting models were then assembled by transplanting the individually refined parts (RNCs and factors recruited by NAC) into homogeneously refined EM maps, followed by real-space refinement for 1 macrocycle with and 3 macrocycles without secondary structure restraints to remove side chain clashes. The final models were validated using the MolProbity tool implemented in Phenix<sup>59</sup> and display good geometry and model-to-map fits (Extended Data Table 1 and Extended Data Fig. 3). The locally refined EM maps were aligned with and resampled on grids of respective homogeneously refined EM maps using ChimeraX for real-space refinements; the resampled maps were deposited on Electron Microscopy Data Bank (EMDB) as supplementary maps for the locally refined maps.

#### C. elegans and human cell experiments

Strains and transformation. Wild-type Bristol N2 strain was obtained from Caenorhabditis Genetics Center. Worms were cultured according to standard techniques<sup>60</sup> with *E. coli* OP50 as food source at 20 °C. Transgenic strains were generated using standard microinjection protocols<sup>61</sup>. Single-copy transgene integration was performed using the miniMos transposon method<sup>62</sup>. An RNAi-resistant gene encoding C. elegans Naa15 (hpo-29) was designed using a codon adaptation tool<sup>63</sup>. The gene was synthesized by Integrated DNA Technologies with a C-terminal 3×Flag tag and three synthetic introns. The sequence is listed in Supplementary Table 2. The gene was subcloned into the miniMos pCFJ910 vector<sup>62</sup> under control of the endogenous hpo-29 promoter and 3' untranslated region (UTR). A separate fluorescent marker gene (mCherry) was added to the constructs to identify knock-in worms. The RNAi-resistant construct for C. elegans NACα was described previously<sup>3,33</sup>. Transgenic strain expressing a NatA model substrate was generated by single-copy integration of a YFP reporter gene containing the first twelve N-terminal residues of human SNAP25 (1MAEDADMR-NELE<sup>12</sup>) and a C-terminal 3×HA tag. The SNAP25-YFP-3×HA transgene was driven by the ubiquitous icd-2 promoter and 3' UTR. HYPK knockout strain (VC440) carrying a large deletion in the C. elegans HYPK orthologue F13G3.10 (allele gk228) was obtained from Caenorhabditis Genetics Center. Worms were studied in the embryonal, larval and adult stage. Randomization and blinding were not performed in the C. elegans experiments. Detailed strain information is available in Supplementary Table 3.

**RNA**i. RNAi constructs targeting *C. elegans* endogenous genes (NAC $\alpha$ , *icd-2*; Naa15, *hpo-29*) were cloned by inserting the spliced coding sequences into vector L4440 (Addgene plasmid #1654). Constructs were then transformed into the RNAi feeding *E. coli* strain HT115 containing a modified lac operon for IPTG-induced expression of double-stranded RNA (dsRNA)<sup>64</sup>. For silencing of endogenous genes, synchronized L1 larvae were fed RNAi bacteria for 2 days until the L4/young adult stage. Bacteria were induced with 1 mM IPTG in LB media for 2 h at 30 °C before feeding to worms. Control worms were fed IPTG-induced HT115 bacteria containing the empty L4440 vector. At least three independent biological replicates of all *C. elegans* RNAi experiments were performed.

NatA reporter analysis. Transgenic worms expressing the SNAP25-YFP-3×HA reporter were grown from hatching on RNAi plates for 2 days at 23 °C. Worms were extracted in SDS lysis buffer (62.5 mM Tris pH 6.8,1 mM EGTA, 2% SDS, 1× protease inhibitor cocktail (Roche)) by sonication and boiling for 5 min at 99 °C. Total amount of SNAP25-YFP-3×HA substrate was detected by immunoblotting using a rabbit anti-HA antibody (Covance, PRB-101P). HA antibody was removed by incubating the membrane in mild antibody stripping buffer (1.5% glycine, 0.1% SDS, 1% Tween-20 pH 2.2). N-terminally acetylated substrate levels were then detected by immunoblotting using the SMI antibody, which specifically recognizes the N-terminally acetylated epitope on SNAP25 (BioLegend, 836304)<sup>37</sup>.

**Progeny viability analysis.** Worms were grown on plates containing respective RNAi bacteria from hatch at 20 °C. At least 20 animals were used per condition and their progeny was scored until day 4 of adulthood. Each group was analysed in three independent biological replicates.

**Ribosome binding analysis.** Ribosome sedimentation analysis was performed as previously described<sup>3,34</sup>. In brief, worms were extracted

in ribosome sedimentation buffer (30 mM HEPES-KOH pH 7.4,100 mM potassium acetate, 5 mM MgCl $_2$ , 5% mannitol, 100 µg ml $^{-1}$  cycloheximide, 2 mM  $\beta$ -mercaptoethanol, 1× protease inhibitor cocktail (Roche)), and lysates were cleared by centrifugation and filtration of the supernatant through a 0.45-µm nitrocellulose membrane. Ribosomes were pelleted by ultracentrifugation (200,000g) through a 25% sucrose cushion for 2 h at 4 °C. Proteins in the total and ribosome pellet fractions were then analysed by standard SDS-PAGE and immunoblotting techniques.

**Human cell culture.** Ribosome binding analyses in human cells were performed as previously described<sup>34</sup>. In brief, HEK293T cells (RRID: CVCL 0063) were cultured in Dulbecco's Modified Eagle's Medium (DMEM) supplemented with 10% fetal calf serum (FCS) and 100 µg ml<sup>-1</sup> Normocin in a 5% CO<sub>2</sub> atmosphere at 37 °C. Cells were transfected with DNA and/or small interfering RNA (siRNA) by electroporation in OptiMEM using a NEPA21 electroporator (Nepagene). To knock down NACα and Naa15, cells were transiently transfected with 1 µg siRNA duplex (Biomers) targeting the 3' UTR of NAC $\alpha$  (5'-AGGAGUAACUGCAGCUUGG-dTdT-3') and Naa15 (5'-GCUGCAUUGCUCUAACUUA-dTdT-3'), respectively. Control cells were transfected with 1 µg nonsense siRNA (5'-UUCUCCGAACGU GUCACGU-dTdT-3'). NACα and Naa15 expression was restored in knockdown cells by co-transfection of plasmids expressing N-terminally 3×Flag-tagged NACα and C-terminally 3×Flag-tagged Naa15 variants, respectively, from the CMV promoter and SV403' UTR. Cells were collected 2 days after transfection and extracted in ice-cold lysis buffer (30 mM HEPES-KOH pH 7.4, 100 mM potassium acetate, 5 mM MgCl<sub>2</sub>, 5% mannitol, 0.04% Nikkol, 100 μg ml<sup>-1</sup> cycloheximide, 1 mM DTT, 1× protease inhibitor cocktail (Roche)). Ribosomes were pelleted by ultracentrifugation (220,000g) through a 25% sucrose cushion (prepared in lysis buffer) for 1.5-2 h at 4 °C. Proteins in the ribosomal pellet were then analysed by standard SDS-PAGE and immunoblotting techniques.

Antibodies. The following antibodies were used for immunoblotting: anti-Naa15 (clone D-7) (Santa Cruz, sc-365931, 1:1,000 dilution); anti-Naa10 (clone A-10) (Santa Cruz, sc-373920, 1:1,000 dilution) anti-uS10 (clone EPR8716) (Abcam, ab133776, 1:1,000 dilution); anti-uL4 (clone RQ-7) (Santa Cruz, sc-100838, 1:2,000 dilution); anti-SNAP25 (clone Smi81) (BioLegend, 836304, 1:1,000 dilution); anti-Tubulin (clone AA4.3) (DSHB, 1:20 dilution); anti-HA (Covance, PRB-101P, 1:1,000 dilution); anti-Flag (polyclonal) (Sigma-Aldrich, F7425, 1:1,000 dilution); anti-Flag (clone M2) (Sigma-Aldrich, F1804, 1:1,000 dilution); anti-C. elegans NAC (polyclonal) (in house, 1:5,000 dilution); anti-RPL10 (polyclonal) (Abcepta, AP19053a; 1:2,000 dilution); Goat anti-Rabbit (Licor, IRDye 680RD; 1:20,000 dilution) and Goat anti-Mouse (Licor, IRDye 800CW; 1:15,000 dilution).

# Reporting summary

Further information on research design is available in the Nature Portfolio Reporting Summary linked to this article.

#### **Data availability**

Models and electron microscopy maps were deposited at the PDB and EMDB with accession codes 9F1B, EMD-50124 (homogeneously refined cryo-EM map), EMD-50127 (locally refined cryo-EM map) and EMD-50130 (8OS-NAC-NatA/E cryo-EM map) for the ternary complex, 9F1C,

EMD-50125 (homogeneously refined cryo-EM map) and EMD-50128 (locally refined cryo-EM map) for the quaternary complex, and 9F1D, EMD-50126 (homogeneously refined cryo-EM map) and EMD-50129 (locally refined cryo-EM map) for the quaternary HYPK complex. Each EMDB entry holds either a homogeneously refined map or a locally refined map together with a set of lowpass-filtered or resampled maps presented throughout the manuscript as supplementary maps.

- Liszczak, G. et al. Molecular basis for N-terminal acetylation by the heterodimeric NatA complex. Nat. Struct. Mol. Biol. 20, 1098–1105 (2013).
- Yin, J., Lin, A. J., Golan, D. E. & Walsh, C. T. Site-specific protein labeling by Sfp phosphopantetheinyl transferase. *Nat. Protoc.* 1, 280–285 (2006).
- 48. Sharma, A., Mariappan, M., Appathurai, S. & Hegde, R. S. in *Protein Secretion*, Vol. 619 (ed. Economou, A.) 339–363 (Humana Press, 2010).
- Yin, J. et al. Genetically encoded short peptide tag for versatile protein labeling by Sfp phosphopantetheinyl transferase. Proc. Natl Acad. Sci. USA 102, 15815–15820 (2005).
- Walker, K. W. & Bradshaw, R. A. Yeast methionine aminopeptidase I. Alteration of substrate specificity by site-directed mutagenesis. J. Biol. Chem. 274, 13403–13409 (1999).
- Gottlieb, L. & Marmorstein, R. Biochemical and structural analysis of N-terminal acetyltransferases. Methods Enzymol. 626, 271–299 (2019).
- Jarmoskaite, I., AlSadhan, I., Vaidyanathan, P. P. & Herschlag, D. How to measure and evaluate binding affinities. eLife 9. e57264 (2020).
- Zivanov, J. et al. New tools for automated high-resolution cryo-EM structure determination in RELION-3. eLife 7, e42166 (2018).
- Punjani, A., Rubinstein, J. L., Fleet, D. J. & Brubaker, M. A. cryoSPARC: algorithms for rapid unsupervised cryo-EM structure determination. *Nat. Methods* 14, 290–296 (2017).
- Rosenthal, P. B. & Henderson, R. Optimal determination of particle orientation, absolute hand, and contrast loss in single-particle electron cryomicroscopy. J. Mol. Biol. 333, 721-745 (2003).
- Pettersen, E. F. et al. UCSF ChimeraX: structure visualization for researchers, educators, and developers. Protein Sci. 30, 70–82 (2021).
- Emsley, P., Lohkamp, B., Scott, W. G. & Cowtan, K. Features and development of Coot. Acta Crystallogr. D 66, 486–501 (2010).
- Liebschner, D. et al. Macromolecular structure determination using X-rays, neutrons and electrons: recent developments in Phenix. Acta Crystallogr. D 75, 861–877 (2019).
- Chen, V. B. et al. MolProbity: all-atom structure validation for macromolecular crystallography. Acta Crystallogr. D 66, 12–21 (2010).
- 60. Brenner, S. The genetics of Caenorhabditis elegans. Genetics 77, 71-94 (1974).
- 61. Mello, C. & Fire, A. DNA transformation. Methods Cell Biol. 48, 451-482 (1995).
- Frøkjær-Jensen, C. et al. Random and targeted transgene insertion in Caenorhabditis elegans using a modified Mos1 transposon. Nat. Methods 11, 529–534 (2014).
- Redemann, S. et al. Codon adaptation-based control of protein expression in C. elegans. Nat. Methods 8, 250–252 (2011).
- Ketting, R. F., Tijsterman, M. & Plasterk, R. H. A. Introduction of double-stranded RNA in C. elegans by feeding. CSH Protoc. 2006, pdb.prot4317 (2006).

Acknowledgements We thank R. Marmorstein and L. Gottlieb for expression plasmids for NatA/E and HYPK; M. Leibundgut and M. Jaskolowski for advice on model building, cryo-EM data processing and feedback on the manuscript; the ETH Scientific Center for Optical and Electron Microscopy (ScopeM) for technical support; L. Hang, G. Hunaeus and R. Schloemer for technical assistance; and members of the Shan laboratory for feedback on the manuscript. This work was supported by National Institutes of Health grant R35 GM136321 and National Science Foundation grant 2219287 to S.-o.S., the German Science Foundation grants SFB969/AO1/AO7 and 537004599 to E.D. and M.G., and the Swiss National Science Foundation (SNSF grant 310030\_212308 to N.B.), the National Center of Excellence in Research RNA & Disease Program of the SNSF (grant 51NF40-205601 to N.B.), and the European Research Council (Synergy Grant 101072047 CoTransComplex to N.B.).

Author contributions A.M.L. and S.-o.S. conceived the project. A.M.L., S.-o.S., D.Y., N.B., M.G. and E.D. designed research. A.M.L. and S.C. performed biochemical experiments and analysed data, D.Y., A.S. and N.B. performed cryo-EM studies. M.G. and L.R. performed studies in C. elegans and human cells. S.-o.S., N.B. and E.D supervised the project. A.M.L. and D.Y. wrote the manuscript. S.-o.S., N.B., E.D. and M.G. revised and edited the manuscript.

 $\textbf{Competing interests} \ \mathsf{The \ authors \ declare \ no \ competing \ interests}.$ 

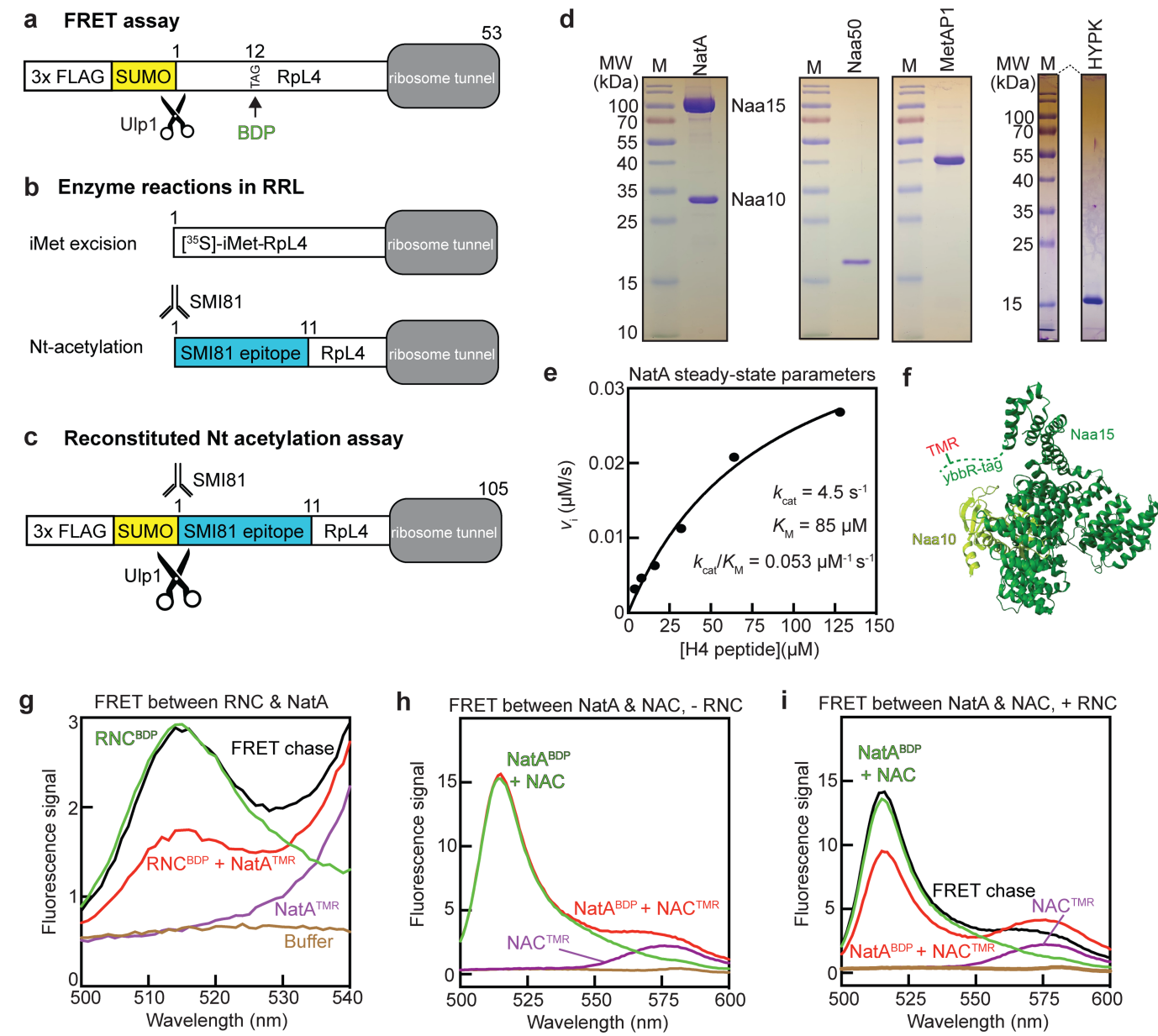
#### Additional information

**Supplementary information** The online version contains supplementary material available at https://doi.org/10.1038/s41586-024-07846-7.

Correspondence and requests for materials should be addressed to Nenad Ban or Shu-ou Shan.

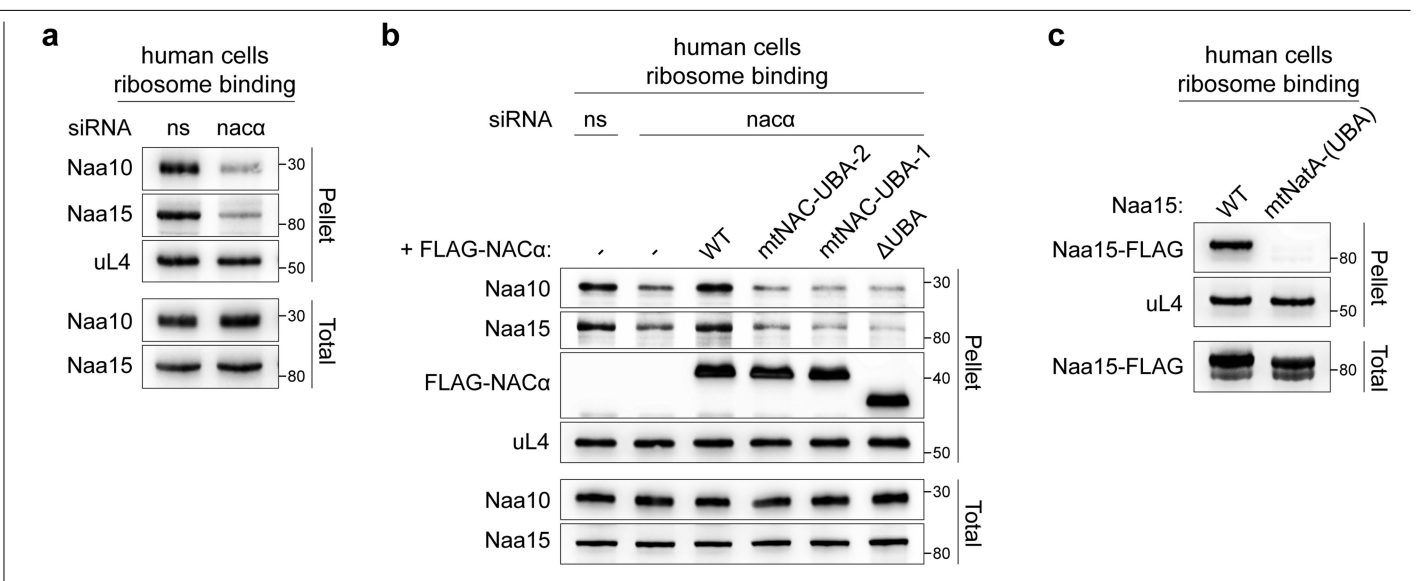
**Peer review information** *Nature* thanks the anonymous reviewer(s) for their contribution to the peer review of this work. Peer review reports are available.

Reprints and permissions information is available at http://www.nature.com/reprints.



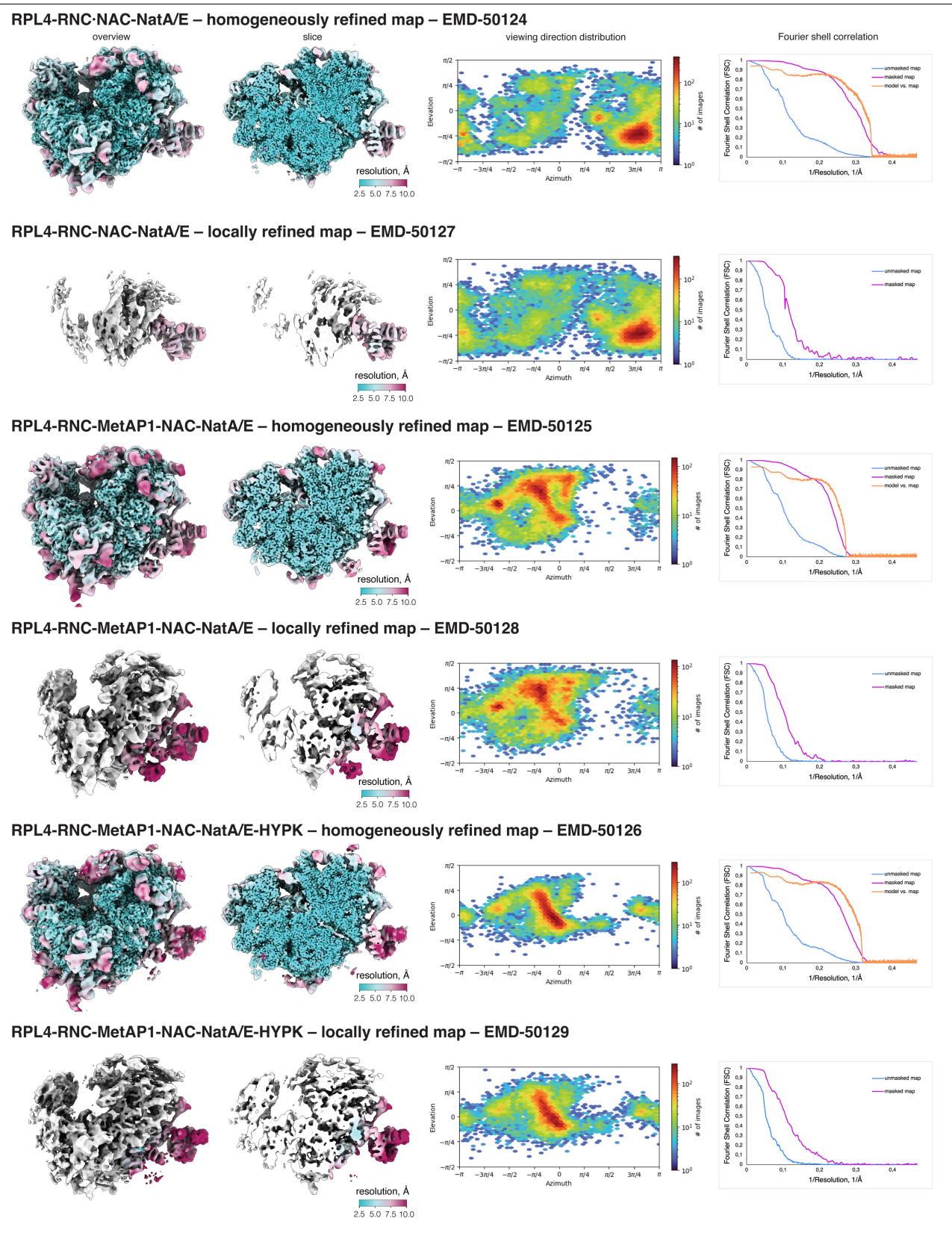
#### Extended Data Fig. 1|FRET of NatA with RNC and with NAC on the ribosome. (a-c) Scheme of the nascent chain constructs used in this work. Grev depicts the ribosome exit tunnel up to the PTC. The nascent chain for FRET between RNC and NatA (a) contains an N-terminal 3xFLAG tag, SUMO, and residues 1-53 of the RpL4 nascent chain with Met1 mutated to serine. An amber codon at residue 12 allows for fluorescence labeling using BODIPY-FL (BDP). After FLAG affinity purification, SUMO cleavage by Ulp1 generates a 53 amino acid (aa) long nascent chain with a defined N-terminus recognized by NatA. Nascent chains for enzymatic assays in RRL are shown in (b). Constructs to measure iMet excision (upper) contained varying lengths of RpL4 with a single iMet, which was radioactively labeled with [35S] and detected via autoradiography. Constructs to measure Nt-acetylation (lower) contained residues 2-12 from SNAP25, which is specifically detected by the SMI antibody upon Nt-acetylation (SMI81 epitope), followed by varying lengths of the RpL4 nascent chain. The nascent chain for measurement of Nt-acetylation reconstituted with purified RNC and proteins is shown in (c) and contains an N-terminal 3xFLAG tag, SUMO, the SMI81 epitope, a GSGS linker, and residues 1-90 of the RpL4 nascent chain. After purification of RNC, SUMO cleavage by Ulp1 generates a defined N-terminus for acetylation. (d) Purified proteins (as indicated) were visualized on a 12.5% SDS-PAGE gel and Coomassie Blue staining. The dashed line indicates that the two lanes were from the same gel. Similar protein quality was observed

from 2, 1, 3, and 2 independent preparations of NatA, Naa50, MetAP1, and HYPK, respectively. (e) Steady-state kinetics of WT human NatA expressed and purified from S. cerevisiae. Reactions contained the indicated concentrations of the H4 peptide substrate (SGRGKGGKGLGKGGAKRHR), 20 µM [14C]-acetyl-CoA, 80 μM [<sup>12</sup>C]-acetyl-CoA, and 10 nM NatA. The progress of the reaction was monitored in the linear range (<10% of product formation). The concentration dependence of initial rates was fit to the Michaelis-Menten equation to obtain the steady-state parameters. (f) The position of the N-terminal ybbR tag and the site of acceptor dye (TMR) label are shown on the human NatA structure (PDB: 6C9M) using a dotted line. Naa15 and Naa10 are colored in dark and light green, respectively. The figure was generated with Pymol v.2.5.5. (g) Fluorescence emission spectra of RNC  $^{BDP}$  with the 53 aa long RpL4  $nascent\, chain\, (\textit{green}), Nat A^{\text{TMR}}\, (\textit{purple}), RNC^{\text{BDP}}\, with\, Nat A^{\text{TMR}}\, (\textit{red}), and$ RNCBDP • NatATMR chased with excess unlabeled NatA (black). Where indicated, the reactions contained 1 nM RNC  $^{\text{BDP}}$  , 100 nM NatA  $^{\text{TMR}}$  , and 1  $\mu\text{M}$  unlabeled NatA. (h, i) Fluorescence emission spectra measuring FRET between NatABDP and NAC<sup>TMR</sup> in the absence (h) or presence (i) of 5 nM unlabeled RNC with a 53 aa long RpL4 nascent chain. 5 nM NatA $^{BDP}$  + 5 nM unlabeled NAC are shown in green, 5 nM NatA  $^{\rm BDP}$  + 5 nM NAC  $^{\rm TMR}$  in red, 5 nM NAC  $^{\rm TMR}$  alone in purple, 5 nM  $NatA^{BDP}$  + 5 nM NAC  $^{TMR}$  + 250 nM unlabeled NAC in *black*, and buffer only in brown.



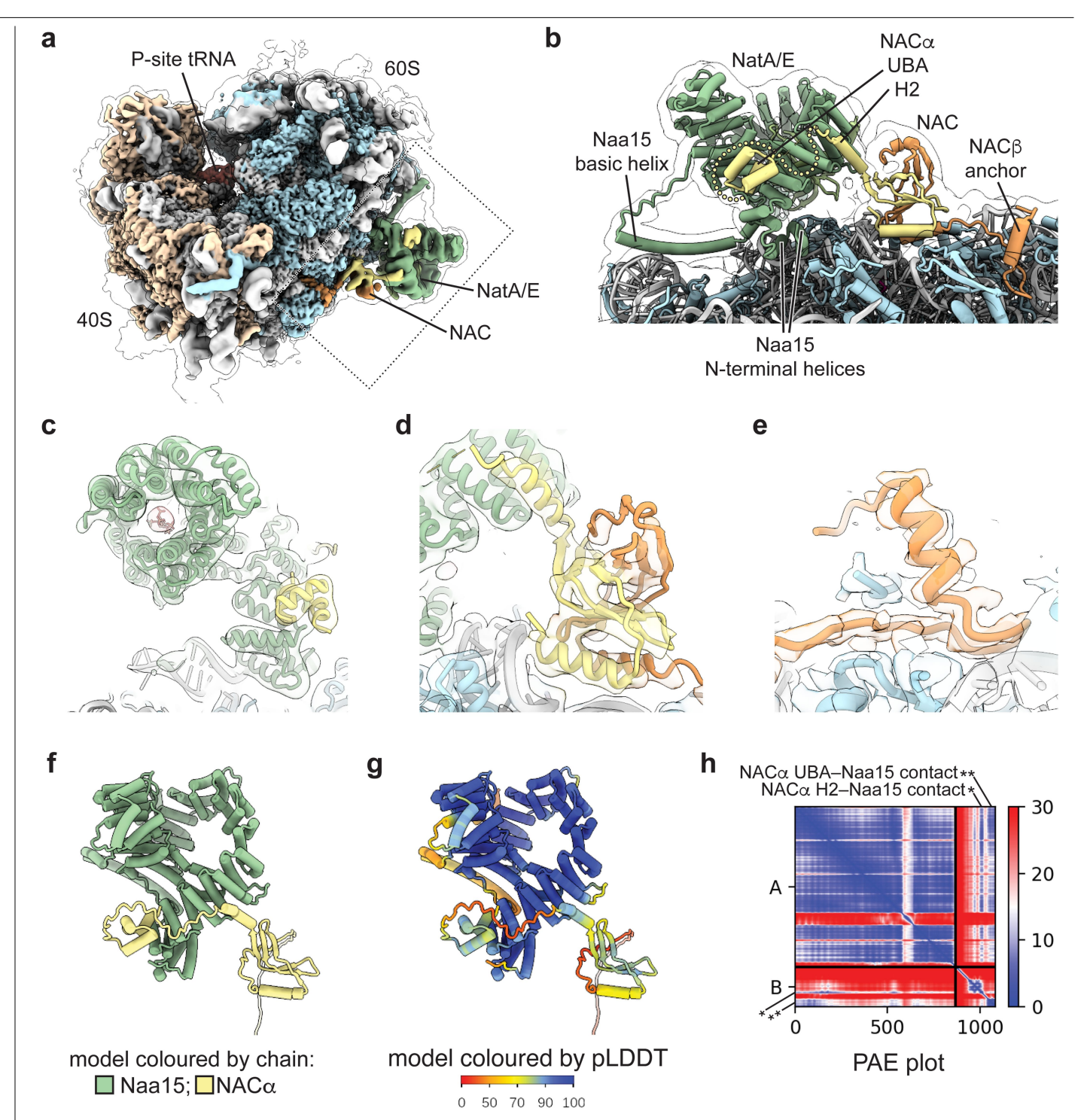
**Extended Data Fig. 2** | **Ribosome binding of NatA in human cells depends on NAC.** (a) Ribosome association of NatA after knockdown of NAC $\alpha$  in human HEK293T cells. Total and ribosomal pellet fractions were analyzed by immunoblotting. ns, nonsense siRNA control. Representative immunoblot is shown. Experiment was repeated three times. (b) Ribosome association of NatA after knockdown of NAC $\alpha$  in human HEK293T cells using siRNAs targeting the endogenous NAC $\alpha$  mRNA in the 3' UTR. NAC $\alpha$  expression was restored in knockdown cells by transient expression FLAG-tagged NAC $\alpha$  variants from plasmids containing a different 3' UTR. Two NAC $\alpha$  variants carrying point mutations in the NAC $\alpha$  UBA-Naa15 binding interface (mtNAC-UBA-1 and -2;

see Extended Data Table 2) and a deletion mutant lacking the entire UBA domain ( $\Delta$ UBA; see Extended Data Table 2) were analyzed. ns, nonsense siRNA control. Representative immunoblot is shown. Experiment was repeated three times. (c) Ribosome association of FLAG-tagged Naa15 variants in human HEK293T cells in the endogenous Naa15 knockdown background. A mutant variant carrying three point mutations in the hydrophobic NAC $\alpha$ UBA binding interface (L73A/L77A/W83A) was compared with wildtype Naa15. Total and ribosomal pellet fractions were analyzed by immunoblotting. Representative immunoblot is shown. Experiment was repeated three times.



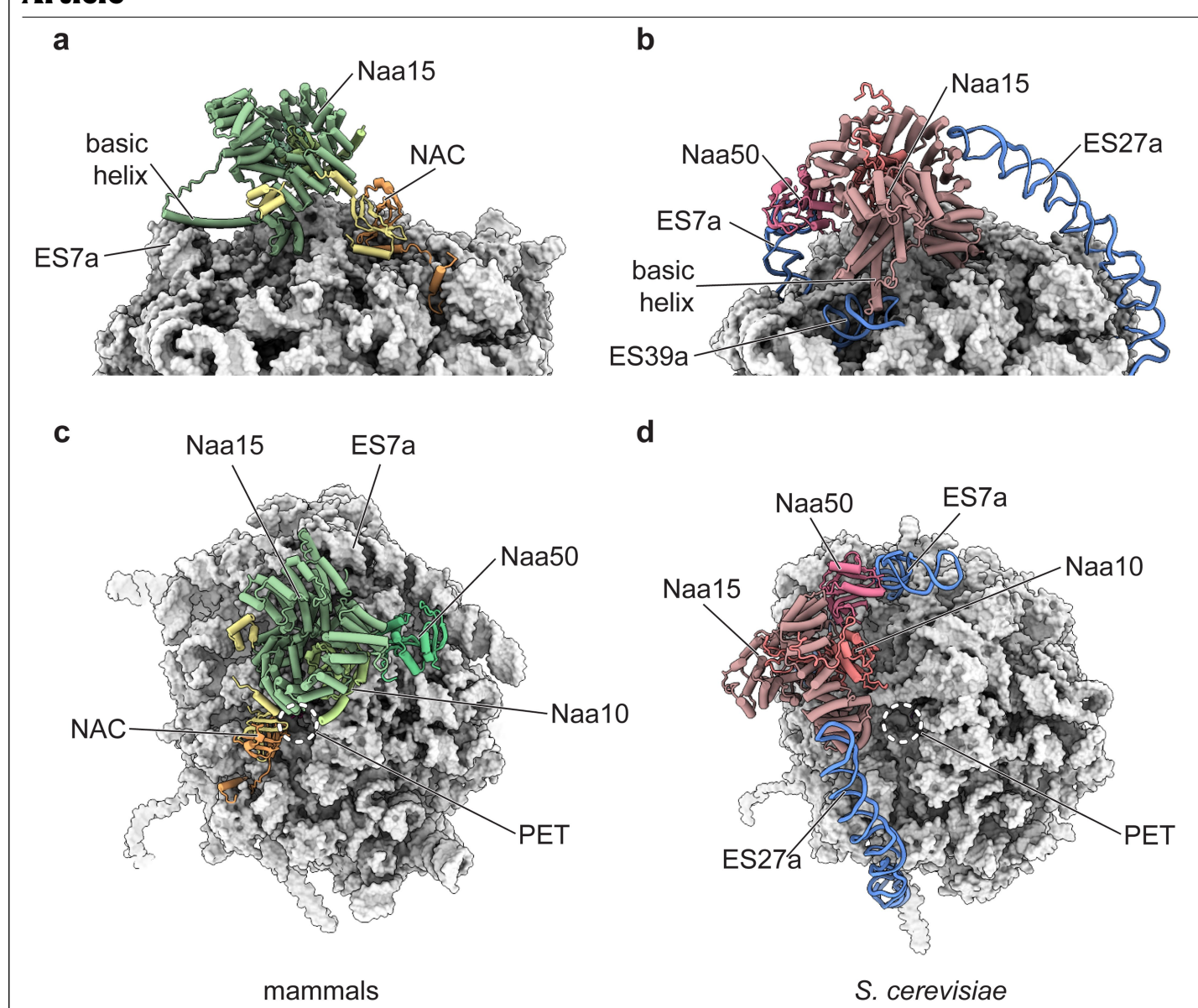
**Extended Data Fig. 3** | **Local resolution estimates, orientation distribution** and refinement statistics of cryo-EM maps. Each row shows, from the left to right: an overview and slice-through of the cryo-EM map, both filtered and coloured according to estimated local resolution, a viewing direction distribution heatmap, and Fourier shell correlations (between unmasked or masked half maps – blue and purple curves, respectively; between the map and the model after the final round of refinement – orange curves). The local

resolution estimation and filtering was done in CryoSPARC. Maps were coloured on the same scale from 2.5 to  $10\,\text{\AA}$ . The viewing direction distribution for each map was taken from corresponding CryoSPARC refinement outputs. For locally refined maps, only areas within refinement masks were coloured. The FSC curves for maps and map vs. model were obtained from outputs of map refinements in CryoSPARC and real-space refinements of models in Phenix, respectively.



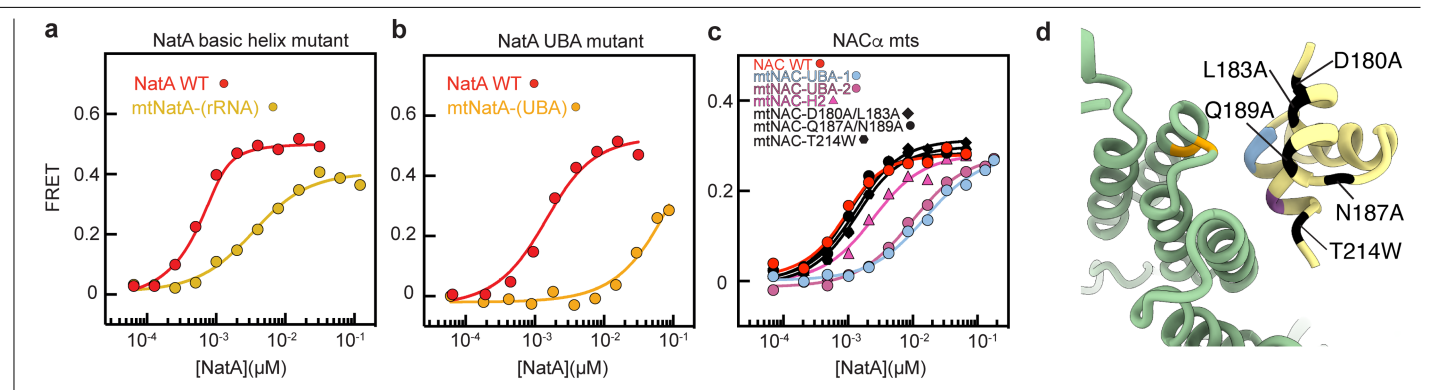
**Extended Data Fig. 4** | **Cryo-EM structure and model of the RNC**  $_{\text{RpL4}}$ -**NAC-NatA/E ternary complex. (a)** Front view of the cryo-EM map of RNC  $_{\text{RpL4}}$ -bound with NAC and NatA/E. The map shows the NatA/E complex bound to the large ribosomal subunit next to the globular domain of NAC. The map was lowpass-filtered to the estimated local resolution. The black outline shows the same map lowpass-filtered to 8 Å resolution. (b) Detailed view of the ternary complex model depicted in (A) showing NatA/E and NAC on the 60 S ribosomal subunit. The yellow dotted line represents the flexible linker between NAC $\alpha$  helix H2 and the UBA domain. NatA/E contacts the ribosome through its Naa15 auxiliary subunit via patches of positively charged residues within the basic helix of Naa15 and N-terminal helices that bind to the backbone of ribosomal RNA. The NAC $\alpha$  C-terminal tail forms a bipartite contact with Naa15 with its UBA domain and H2. **(c-e)** Details of cryo-EM maps of the ternary complex showing a segment of Naa15 in contact with the NAC $\alpha$  UBA domain (c), the

NAC $\alpha$ -H2 density connecting to the globular domain of NAC (d), and the N-terminal ribosome anchor of NAC $\beta$  (e). The locally refined map (c), the homogeneously refined map lowpass filtered to 6 Å resolution (d) and the homogeneously refined map (e) are displayed as semi-transparent surfaces. (f-h) ColabFold-predicted dimer model of the Naa15-NAC $\alpha$  complex. The AlphaFold model is coloured by chain (f), with Naa15 in green and NAC $\alpha$  in yellow, and by the pLDDT confidence score (g). (h) shows the predicted Aligned Error (PAE) plot for the predicted model, with Naa15 as chain A and NAC $\alpha$  as chain B. The chain residues are marked along the x and y axis, and the heatmap indicates the estimated position error (in Å) for residue x when predicted and true structures are aligned on residuey. Low PAE for residue pairs from NAC $\alpha$  UBA and Naa15 (marked on the plot with \*) and NAC $\alpha$  H2 and Naa15 (marked as \*\*) indicate that the relative positions of corresponding domains are well-defined in the AlphaFold prediction.



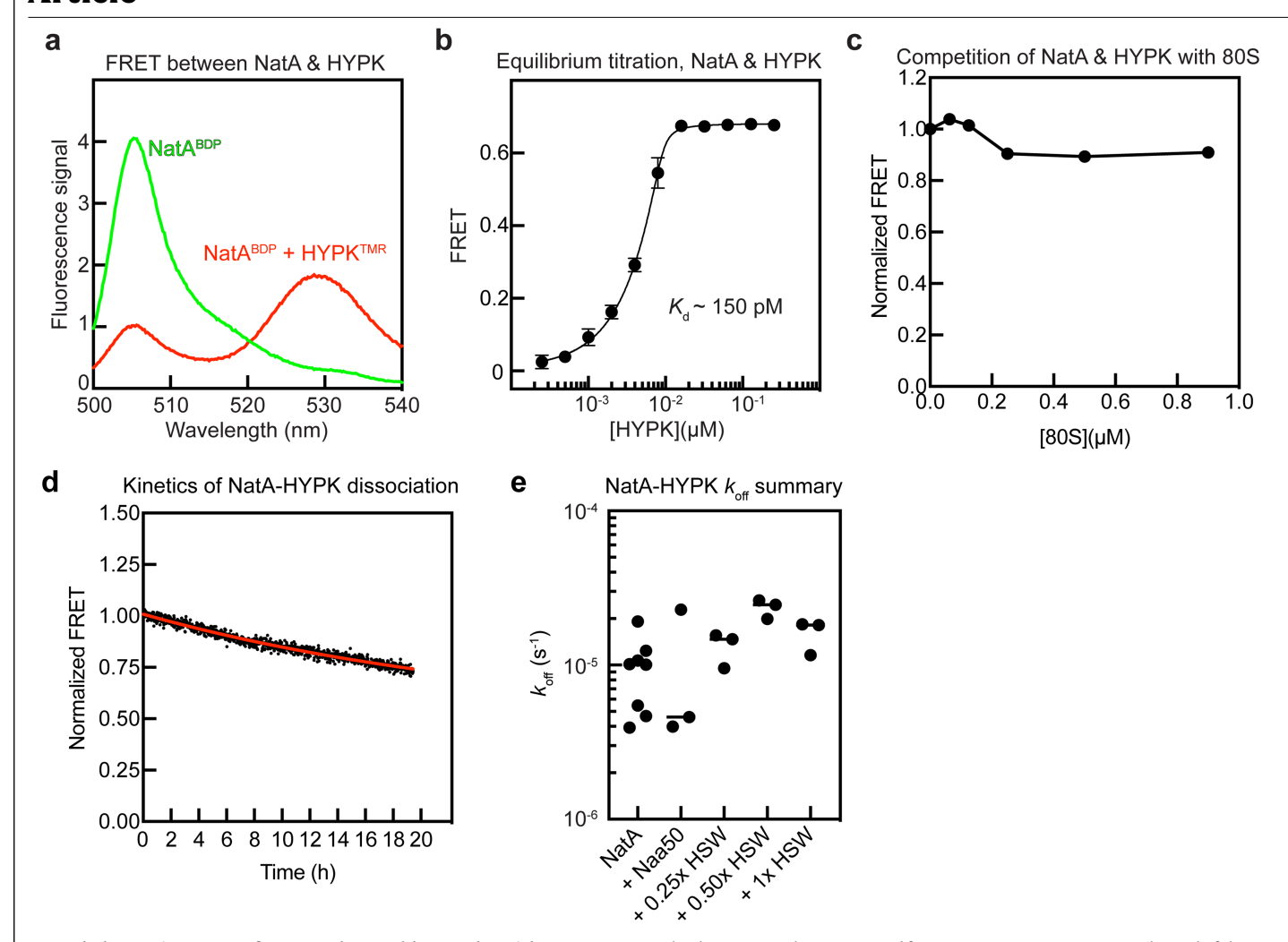
**Extended Data Fig. 5** | **Mammals and yeast employ distinct modes of NatA/E recruitment to ribosomes.** Side ( $\mathbf{a}$ ,  $\mathbf{b}$ ) and top ( $\mathbf{c}$ ,  $\mathbf{d}$ ) views of the mammalian ternary RNC<sub>RpL4</sub>-NAC-NatA/E complex ( $\mathbf{a}$ ,  $\mathbf{c}$ ) and those of the yeast RNC-NatA/E complex ( $\mathbf{b}$ ,  $\mathbf{d}$ ; PDB# 6HD5). The ribosomes are shown in surface representation, bound factors and selected expansion segments in cartoon. The NAC heterodimer is shown in yellow and orange, mammalian NatA/E in hues of green, rRNA expansion segments coordinating NatA/E in blue, and yeast NatA/E in hues of pink. While the N-terminal helical domain of Naa15 contacts the ribosome near the exit tunnel in both mammalian and yeast systems, all other structural elements that mediate NatA recruitment and positioning on the ribosome are distinct in the two organisms. Firstly, ribosome-bound NAC captures and helps position NatA/E in mammals, whereas in yeast, the rRNA

extension Es27 is proposed to act as a protein recruitment hub for NatA in place of NAC. Secondly, the second catalytic subunit Naa50 mediates an additional contact with the rRNA extionsion Es7a on the yeast ribosome, whereas Naa50 is not involved in ribosome contact and hence does not contribute to the ribosome affinity of mammalian NatA/E as shown in Fig. 1. Thirdly, the locations of the NatA/E complex at the ribosome exit site are distinct in the two organisms. Finally, the ribosome binding site of mammalian NAC heavily overlaps with that of yeast NatA/E, suggesting that yeast NAC antagonizes rather than facilitates the ribosome recruitment of NatA/E. These differences, together with the absence of the NatA regulator HYPK in *S. cerevisiae*, suggest that the ribosome recruitment mechanisms for protein biogenesis factors are distinct between yeast and higher eukaryotic organisms.



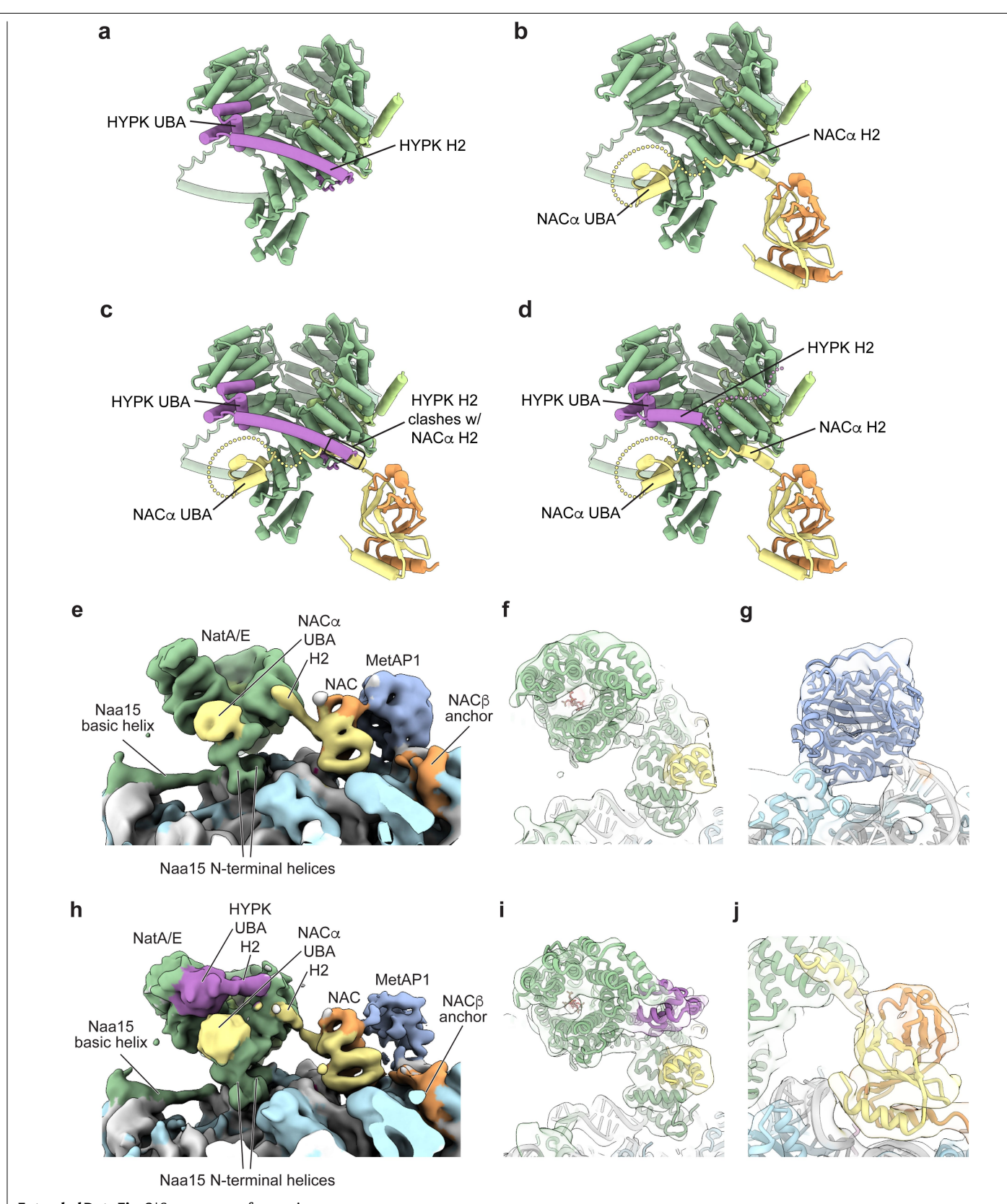
Extended Data Fig. 6 | Equilibrium titrations to measure the binding of NatA to RNC•NAC with the indicated NAC or NatA variants. (a-c) Titrations contained 1 nM RNC BDP, indicated concentrations of WT NatA TMR or NatA TMR

variants (a, b), and 50 nM NAC WT or NAC variants (c). (d) Close-up view of the interaction between Naa15 TPR and the NAC  $\alpha$  UBA domain. Mutated residues are colored as in (b) and (c).



**Extended Data Fig. 7** | **HYPK forms an ultra-stable complex with NatA.**(a) Fluorescence emission spectra of 5 nM NatA  $^{\text{BDP}}$  with (red) and without (green) 50 nM HYPK  $^{\text{TMR}}$ . (b) Equilibrium titrations to measure the binding of NatA  $^{\text{BDP}}$  to HYPK  $^{\text{TMR}}$ . Data are shown as mean  $\pm$  SD, with n = 3 independent measurements. (c) FRET between NatA-HYPK was not changed by increasing concentrations of the 80 S ribosome. (d) Kinetics of dissociation of NatA-HYPK. The line is a fit of

the data to a single exponential function assuming FRET = 0 at the end of the reaction. (e) Summary of the dissociation rate constant of the NatA-HYPK complex, in the absence and presence of the additional Naa50 catalytic subunit or by increasing the concentration of the ribosome high-salt wash fraction (HSW). Individual data points for independent measurements are shown.



 $\textbf{Extended Data Fig. 8} | See \ next \ page \ for \ caption.$ 

Extended Data Fig. 8 | Structural modeling and cryoEM analysis of HYPK bound to NatA on the RNC-NAC complex. (a-d) HYPK H2 in inhibitory conformation would clash with bound H2 of NACα. In (a), the model of HYPK from NatA-HYPK complex (PDB 6C95) is superimposed on the model of NatA/E from the quaternary RNC-NAC-NatA/E-MetAP1 complex. Models were aligned by Naa15, only HYPK from the isolated NatA-HYPK complex is displayed. (b) shows the model of NAC-NatA/E from the quaternary RNC-NAC-NatA/E-MetAP1 complex. (c) shows the model of HYPK from NatA-HYPK complex (PDB 6C95) superimposed on the model of NAC-NatA/E from the quaternary RNC-NAC-NatA/E-MetAP1 complex. The binding site of HYPK H2 in its inhibitory conformation on Naa15 in part overlaps with that of H2 of NACα, when NatA/E is recruited to the ribosome. (d) shows a model of NatA/E-HYPK-NAC from the quaternary complex with HYPK. The N terminus of HYPK is remodelled upon

recruitment to the ribosome by NAC. The flexible linker connecting NAC  $\alpha$  H2 and UBA and displaced HYPK N terminus are shown as yellow and purple dotted lines, respectively. (**e-j**) Comparison between cryo-EM maps of quaternary complexes with and without HYPK. e-g, details of the locally refined cryo-EM map of the quaternary complex showing the front view of the quaternary complex (e), a segment of Naa15 with NAC  $\alpha$  UBA (f), and MetAP1(g). h-j, details of the locally refined cryo-EM map of the quaternary complex with HYPK showing the front view of the complex (h) and a segment of Naa15 with NAC  $\alpha$  UBA and HYPK UBA (i). A detail of a homogeneously refined map, lowpass filtered to 6 Å resolution, shows how NAC  $\alpha$ -H2 connects to the globular domain of NAC (j). The maps are displayed as solid surfaces (e, h) or as semi-transparent surfaces superimposed on models of the complexes (f-g, i-j). Colors are the same as in Fig. 1e, with MetAP1 in blue-grey and HYPK in purple.

# Extended Data Table 1 | Cryo-EM data collection, refinement and validation statistics

	Ternary complex – RNC-NAC-NatA/E EMD-50124 PDB 9F1B	Ternary complex – local refinement EMD-50127	Temary complex – 80S-NAC- NatA/E EMD-50130	Quatemary complex – RNC-NAC-MetAP1- NatA/E EMD-50125 PDB 9F1C	Quaternary complex — local refinement EMD-50128	Quaternary complex w/ HYPK – RNC-NAC-MetAP1- NatA/E-HYPK EMD-50126 PDB 9F1D	Quaternary complex w/ HYPK – local refinement EMD-50129
Data collection and							
processing							
Magnification	x81,000	x81,000	x81,000	x81,000	x81,000	x81,000	x81,000
Voltage (kV)	300	300	300	300	300	300	300
Electron exposure (e-/Å <sup>2</sup> )	60	60	60	50	50	50	50
Defocus range (µm)	-2.4 to -0.6	-2.4 to -0.6	-2.4 to -0.6	-2.4 to -0.6	-2.4 to -0.6	-2.4 to -0.6	-2.4 to -0.6
Pixel size (Å)	1.06	1.06	1.06	1.065	1.065	1.06	1.06
Symmetry imposed	C1	C1	C1	C1	C1	C1	C1
Initial particle images (no.)	457,759	457,759	457,759	360,184	360,184	156,452	156,452
Final particle images (no.)	37,182	37,182	20,439	21,864	21,864	23,034	23,034
Map resolution (Å)	3.01	6.45	3.21	3.78	6.67	3.26	5.75
FSC threshold	0.143	0.143	0.143	0.143	0.143	0.143	0.143 5 to 12
Map resolution range (Å)	2.2 to 8	6 to 8	2.2 to 7	2.2 to 10	6 to 10	2.2 to 12	51012
Refinement							
Initial model used (PDB	8P2K, 7QWR,			8P2K, 7QWR, 6PPL,		8P2K, 7QWR, 6PPL,	
code)	6PPL			2B3H		6PW9, 2B3H	
Model resolution (Å)	3.1			3.9		3.4	
FSC threshold	0.5			0.5		0.5	
Map sharpening B factor $(\mathbb{A}^2)$	27.9			58.9		37.1	
Model composition							
Non-hydrogen atoms	234,232			236,684		237,089	
Protein residues	13,274			13,584		13,638	
Nucleotides $B$ factors ( $\mathbb{A}^2$ )	5,830			5,830		5,830	
Protein	33.90/351.72/109.14			51.19/508.02/130.72		33.19/364.56/97.68	
Nucleotides	36.25/639.20/100.84			51.11/1005.02/112.05		35.30/670.83/79.41	
Ligand	35.10/413.36/127.48			51.25/440.34/129.05		33.79/571.90/95.12	
R.m.s. deviations							
Bond lengths (Å)	0.002			0.001		0.001	
Bond angles (°) Validation	0.363			0.360		0.364	
MolProbity score	1.27			1.28		1.24	
Clashscore	5.03			5.22		4.64	
Poor rotamers (%)	0.80			0.69		0.89	
Ramachandran plot							
Favored (%)	98.51			98.73		98.57	
Allowed (%)	1.48			1.26		1.40	
Disallowed (%)	0.02			0.01		0.03	

# Extended Data Table 2 | List of protein mutations used in this work

Protein	Mutant name	Protein region	Species	Mutated amino acid residues
NACα ΔUBA UBA		H. sapiens Deletion of residues 176		
NACα	ΔUBA	UBA	C. elegans	Deletion of residues 158-195
NACα	mtNAC-UBA-1	UBA	H. sapiens	I206A/V207A
NACα	mtNAC-UBA-1	UBA	C. elegans	I186A/V187A
NACα	mtNAC-UBA-2	UBA	H. sapiens	M211A
NACα	D180A/L183A	UBA	H. sapiens	D180A/L183A
NACα	Q187A/N189A	UBA	H. sapiens	Q187A/N189A
NACα	T214W	UBA	H. sapiens	T214W
NACα	mtNAC-H2	Helix 2	H. sapiens	Q136A/K142E/F143A
NACβ	ΔC	C-terminal	H. sapiens	Deletion of residues 140-162
Naa15	mtNatA-(UBA)	TPR	H. sapiens, in vitro	L73A/L77A
Naa15	mtNatA-(UBA)	TPR	H. sapiens, cell line	L73A/L77A/W83A
Naa15	mtNatA-(UBA)	TPR	C. elegans	L80A/L84A/W90A
Naa15	mtNatA-(rRNA)	Basic helix	H. sapiens	K590E/K593E/K594E/R596E/ K598E/R600E/R601E/K604E/ K605E
Naa10	E24Q/Y26F	Active site	H. sapiens	E24Q/Y26F
MetAP1	D220N	Active site	H. sapiens	D220N

# nature portfolio

Corresponding author(s):	Shu-ou Shan
Last updated by author(s):	6/14/2024

# **Reporting Summary**

Nature Portfolio wishes to improve the reproducibility of the work that we publish. This form provides structure for consistency and transparency in reporting. For further information on Nature Portfolio policies, see our <u>Editorial Policies</u> and the <u>Editorial Policy Checklist</u>.

~				
<b>\</b> 1	יביו	tic	ŤΙ	$\sim$

For	all statistical analyses, confirm that the following items are present in the figure legend, table legend, main text, or Methods section.
n/a	Confirmed
	The exact sample size $(n)$ for each experimental group/condition, given as a discrete number and unit of measurement
	A statement on whether measurements were taken from distinct samples or whether the same sample was measured repeatedly
$\boxtimes$	The statistical test(s) used AND whether they are one- or two-sided Only common tests should be described solely by name; describe more complex techniques in the Methods section.
$\boxtimes$	A description of all covariates tested
$\boxtimes$	A description of any assumptions or corrections, such as tests of normality and adjustment for multiple comparisons
	A full description of the statistical parameters including central tendency (e.g. means) or other basic estimates (e.g. regression coefficient AND variation (e.g. standard deviation) or associated estimates of uncertainty (e.g. confidence intervals)
$\boxtimes$	For null hypothesis testing, the test statistic (e.g. <i>F</i> , <i>t</i> , <i>r</i> ) with confidence intervals, effect sizes, degrees of freedom and <i>P</i> value noted <i>Give P values as exact values whenever suitable.</i>
$\boxtimes$	For Bayesian analysis, information on the choice of priors and Markov chain Monte Carlo settings
$\boxtimes$	For hierarchical and complex designs, identification of the appropriate level for tests and full reporting of outcomes
$\boxtimes$	Estimates of effect sizes (e.g. Cohen's <i>d</i> , Pearson's <i>r</i> ), indicating how they were calculated
'	Our web collection on <u>statistics for biologists</u> contains articles on many of the points above.

# Software and code

Policy information about availability of computer code

ColabFold 1.3.0

Data collection

FelixFL v1.0.34.0 (Horiba); EPU 2.10.0.5; 3.0.0.4164 and 3.2.0.4776 (Thermo Fisher)

Data analysis

Prism v 10.1.0 (statistical package), ImageJ 1.53t (image quantification and analysis); Relion 3.1; CryoSPARC v3.32-4.40; Coot v0.9.8.91; Phenix v1.20.1-4487; PYMOL v2.5.5; UCSF Chimera v1.17.2; UCSF Chimera v1.5;

For manuscripts utilizing custom algorithms or software that are central to the research but not yet described in published literature, software must be made available to editors and reviewers. We strongly encourage code deposition in a community repository (e.g. GitHub). See the Nature Portfolio <u>guidelines for submitting code & software</u> for further information.

#### Data

Policy information about availability of data

All manuscripts must include a data availability statement. This statement should provide the following information, where applicable:

- Accession codes, unique identifiers, or web links for publicly available datasets
- A description of any restrictions on data availability
- For clinical datasets or third party data, please ensure that the statement adheres to our policy

All relevant data are presented in the manuscript main text, extended data, and Supplemental Information. Models and EM maps were deposited on PDB and EMDB with accession codes PDB 9F1B, EMD-50124 (homogeneously refined cryo-EM map), EMD-50127 (locally refined cryo-EM map) and EMD-50130 (80S-NAC-NatA/E cryo-EM map) for the ternary complex, PDB 9F1C, EMDB-50125 (homogeneously refined cryo-EM map) and EMD-50128 (locally refined cryo-EM map) for the quaternary complex and PDB 9F1D, EMDB-50126 (homogeneously refined cryo-EM map) and EMD-50129 (locally refined cryo-EM map) for the quaternary-HYPK complex. Each EMDB entry holds a primary map as well as a locally refined map and a set of lowpass filtered or resampled maps presented throughout the manuscript as supplementary maps.

# Research involving human participants, their data, or biological material

,	ut studies with <u>human participants or human data</u> . See also policy information about <u>sex, gender (identity/presentation),</u> and <u>race, ethnicity and racism</u> .				
Reporting on sex and	gender n/a				
Reporting on race, et other socially relevar groupings	···				
Population character	ristics n/a				
Recruitment	n/a				
Ethics oversight	n/a				
Note that full information	on the approval of the study protocol must also be provided in the manuscript.				
Field-speci	ific reporting				
Please select the one b	below that is the best fit for your research. If you are not sure, read the appropriate sections before making your selection.				
Life sciences	Behavioural & social sciences Ecological, evolutionary & environmental sciences				
For a reference copy of the d	ocument with all sections, see <u>nature.com/documents/nr-reporting-summary-flat.pdf</u>				
Life scienc	es study design				
All studies must disclos	se on these points even when the disclosure is negative.				
Sample size Inc	Indicated in figure legends.				
Data exclusions no	no data are excluded				
Replication	number of replicates are indicated in figure legends				
	Randomization is the process of assignment subjects or animals to treatment or control groups. It does not apply in this study (not a clinical trial or drug test)				
Blinding Do	Does not apply as this is not a clinical trial				

# Reporting for specific materials, systems and methods

We require information from authors about some types of materials, experimental systems and methods used in many studies. Here, indicate whether each material, system or method listed is relevant to your study. If you are not sure if a list item applies to your research, read the appropriate section before selecting a response.

Materials & experimental systems		Methods		
n/a	Involved in the study	n/a	Involved in the study	
	X Antibodies	$\boxtimes$	ChIP-seq	
	∑ Eukaryotic cell lines	$\boxtimes$	Flow cytometry	
$\boxtimes$	Palaeontology and archaeology	$\boxtimes$	MRI-based neuroimaging	
	Animals and other organisms	,		
$\boxtimes$	Clinical data			
$\boxtimes$	Dual use research of concern			
$\boxtimes$	Plants			

# **Antibodies**

#### Antibodies used

RPL10 (Abcepta, AP19053a),
SMI81 (anti-SNAP25; BioLegend, 836304),
Goat anti-Rabbit (Licor, IRDye 680RD),
Goat anti-Mouse (Licor, IRDye 800CW),
rabbit anti-HA antibody (Covance, #PRB-101P);
anti-Naa15 (clone D-7), Santa Cruz, sc-365931
anti-uS10 (clone EPR8716), Abcam, ab133776
anti-Tubulin (clone AA4.3), DSHB
anti-FLAG (polyclonal), Sigma-Aldrich, F7425 (used to detect mono FLAG-tagged proteins)
anti-FLAG (clone M2), Sigma-Aldrich, F1804 (used to detect triple FLAG-tagged proteins)

anti-Naa10 (clone A-10), Santa Cruz, sc-373920 anti-uL4 (clone RQ-7), Santa Cruz, sc-100838 anti-C. elegans NACalpha-beta (polyclonal), inhouse produced rabbit antiserum

Validation

RPL10 -- This RPL10 antibody is generated from rabbits immunized with a KLH conjugated synthetic peptide between 17-45 amino acids from the N-terminal region of human RPL10. Purified polyclonal antibody supplied in PBS with 0.09% (W/V) sodium azide. This antibody is purified through a protein A column, followed by peptide affinity purification. Biological Function of Ribosomal Protein L10 on Cell Behavior in Human Epithelial Ovarian Cancer.

Author: Shi J1,Zhang L1,2,Zhou D1,2,Zhang J1,2,Lin Q1,2,Guan W1,Zhang J1,Ren W1,2,Xu G1,2.

J Cancer. 2018 Feb 6;9(4):745-756. doi: 10.7150/jca.21614. eCollection 2018.

SMI81 -- The monoclonal antibody SMI81 binds the Nt-acetylated 11 amino acids of SNAP-25.

Connell et al., "N-Terminal Acetylation of the Neuronal Protein SNAP-25 Is Revealed by the SMI81 Monoclonal Antibody."

Goat anti-Rabbit -- Isolation of specific antibodies was accomplished by affinity chromatography using pooled rabbit IgG covalently linked to agarose. Based on ELISA and flow cytometry, this antibody reacts with the heavy and light chains of rabbit IgG, and with the light chains of rabbit IgM and IgA. This antibody was tested by dot blot and and/or solid-phase adsorbed for minimal cross-reactivity with human, mouse, rat, sheep, and chicken serum proteins, but may cross-react with immunoglobulins from other species. The conjugate has been specifically tested and qualified for Western blot and In-Cell Western™ Assay applications.

Goat anti-mouse -- Isolation of specific antibodies was accomplished by affinity chromatography using pooled mouse IgG covalently linked to agarose. Based on ELISA and flow cytometry, this antibody reacts with the heavy and light chains of mouse IgG1, IgG2a, IgG2b, and IgG3, and with the light chains of mouse IgM and IgA. This antibody was tested by dot blot and and/or solid-phase adsorbed for minimal cross-reactivity with human, rabbit, goat, rat, and horse serum proteins, but may cross-react with immunoglobulins from other species. The conjugate has been specifically tested and qualified for Western blot applications.

rabbit anti-HA antibody (Covance, #PRB-101P) -- The HA tag (hemagglutinin) is an amino acid sequence derived from the human influenza hemagglutinin surface glycoprotein, corresponding to amino acids 98-106. It is commonly used as a tag to facilitate detection, isolation, and purification of proteins. The full amino acid sequence is: YPYDVPDYA.

anti-Naa15 (clone D-7): validated by manufacturer for immunoblot using several human cell lines (e.g. HeLa). Used in 2 publications.

anti-Naa10 (clone A-10), Santa Cruz, sc-373920: validated by manufacturer for immunoblot using several human cell lines (e.g. Jurkat). Used in 6 publications.

anti-uS10 (clone EPR8716), Abcam, ab133776: validated by manufacturerer for immunoblot against human samples. Used in 9 publications.

anti-Tubulin (clone AA4.3), DSHB: used for immunoblotting in over 123 publications across varoius different species (e.g. human, c. elegans, drosophila etc)

anti-FLAG (polyclonal), Sigma-Aldrich, F7425: standard FLAG epitope antibody, used in numerous publications for immunoblotting, species-independent

anti-FLAG (clone M2), Sigma-Aldrich, F1804: standard FLAG epitope antibody, used in numerous publications for immunoblotting, species-independent

anti-uL4 (clone RQ-7), Santa Cruz, sc-100838: validated by manufacturer for immunoblotting using several human cell lines (e.g.

HeLa). Used	d in 11	pub	licatior
-------------	---------	-----	----------

anti-C. elegans NACalphabeta: antiserum raised in rabbits against recombinant C. elegans NACalphabeta complex, validated inhouse for detection of C. elegans NACalpha and NACbeta by immunoblotting. Used in 5 publications.

# Eukaryotic cell lines

Policy information about <u>cell lines and Sex and Gender in Research</u>

Cell line source(s) HEK293T cells (RRID: CVCL\_0063) were from ATCC.

Authentication Cell line was not authenticated.

Mycoplasma contamination Cell lines were negative for mycoplasma.

Commonly misidentified lines (See ICLAC register)

None used.

# Animals and other research organisms

Policy information about <u>studies involving animals</u>; <u>ARRIVE guidelines</u> recommended for reporting animal research, and <u>Sex and Gender in Research</u>

Laboratory animals Caenorhabditis elegans (strains: N2 and VC440); animals were studied in the embryonal, larval, and adult stage.

Wild animals No wild animals are used in this study.

Reporting on sex Not relevant to this study. Only hermaphrodites were analyzed.

Field-collected samples No field collected samples are used in this study.

Ethics oversight n/a

Note that full information on the approval of the study protocol must also be provided in the manuscript.

## **Plants**

Seed stocks n/a

Novel plant genotypes n/a

Authentication n/a